RADIATIVE INTERACTIONS: I. LIGHT SCATTERING AND EMISSION FROM IRREGULAR PARTICLES. II. TIME DEPENDENT RADIATIVE COUPLING OF AN ATMOSPHERE-OCEAN SYSTEM

A Dissertation

by

CHANGHUI LI

Submitted to the Office of Graduate Studies of
Texas A&M University
in partial fulfillment of the requirements for the degree of

DOCTOR OF PHILOSOPHY

August 2006

Major Subject: Physics

RADIATIVE INTERACTIONS: I. LIGHT SCATTERING AND EMISSION FROM

IRREGULAR PARTICLES. II. TIME DEPENDENT RADIATIVE COUPLING

OF AN ATMOSPHERE-OCEAN SYSTEM

A Dissertation

by

CHANGHUI LI

Submitted to the Office of Graduate Studies of
Texas A&M University
in partial fulfillment of the requirements for the degree of

DOCTOR OF PHILOSOPHY

Approved by:

Chair of Committee,	George W. Kattawar
Committee Members,	Chia-Ren Hu
	Ping Yang
	Che-Ming Ko
	Vitaly Kocharovsky
	M. Suhail Zubairy
Head of Department,	Edward S. Fry

August 2006

Major Subject: Physics

ABSTRACT

Radiative Interactions: I. Light Scattering and Emission from

Irregular Particles. II. Time Dependent Radiative Coupling of an

Atmosphere-Ocean System. (August 2006)

Changhui Li, B.S., Peking University;

M.S., Peking University;

M.S., Texas A&M University

Chair of Advisory Committee: Dr. George W. Kattawar

In the first part of this dissertation, radiative interactions with single irregular particles are simulated. We first introduce the basic method and techniques of Finite-Difference Time-Domain method(FDTD), which is a powerful method to numerically solve Maxwell's equations with high accuracy. To improve the efficiency of FDTD, we also develop a parallel FDTD code. Since FDTD can simulate light scattering by arbitrary shape and compositions, we study several radiative interaction cases for single particles in an external plane parallel light source: the surface roughness effects on the scattering, electric and magnetic energy density distribution in irregular particles, and backscattered Mueller images. We also develop an innovative and accurate method to simulate the infinitesimal electric dipole radiation from inside a particle with arbitrary shape and composition. Our research and results are very important to study light scattering by irregular particles, Raman scattering and fluorescence.

In the second part of the dissertation, we study radiative interactions in an atmosphere-ocean system. By using the so called Matrix operator method, not only the radiance of the radiation field, but also the polarization of the radiation field are obtained. Given the single layer information for the atmosphere, time dependent ocean surface shapes, and the ocean with no interface, the Matrix operator method

couples these three layers and provides both the radiance and polarization reaching a certain detector in the time domain, which are essential for atmospheric science and oceanography. Several simple cases are studied by this method to demonstrate its accuracy and robustness. We also show the most difficulties in this method and discuss what one need to do in future research works.

To my family and Wendi

ACKNOWLEDGMENTS

First of all, I thank my advisor Dr. George W. Kattawar. During the past four years, his comprehensive knowledge and innovative ideas were always the most important guidance for my research. Besides, he also impressed on me his diligent work and enthusiasm for science research, which will surely influence my future research life.

I would like to thank Dr. Ping Yang. Although he is listed as a committee member, his role in my research work definitely was as a co-advisor. Many research ideas originated from his suggestions.

I would like to thank all other committee members, Dr. Chia-Ren Hu, Dr. M. Suhail Zubairy, Dr. Che-Ming Ko, and Dr. Vitaly Kocharovsky. Their suggestions for my dissertation were really helpful.

I would like to thank Dr. Pengwang Zhai, and Mr. You Yu, members of my research group. Working within this group was a memorable experience. Everyone generously shared his knowledge and ideas. Many times, I found my mistakes as well as new ideas during discussions with them.

I would like to thank my good friends, Gang Zhao, Li Zhu, Yuan Qian, and many others. It is with those friends that life in College Station was easy and joyful.

Thanks to my dear girlfriend, Wendi, her love and support fill my life with joy and peace.

Finally, sincerest gratitude is owed to my family-my parents, my elder sister and her husband. Their love and support always accompanied me and enabled me to finish this dissertation and obtain the degree.

TABLE OF CONTENTS

LIST OF TABLES

LIST OF FIGURES

FIGURE   Page

FIGURE   Page

CHAPTER I

INTRODUCTION AND BACKGROUND

The scattering of light by irregular particles is essential to atmospheric radiative transfer[1], biological aerosol detection, remote-sensing technology and other disciplines. The light scattering process can be divided into three basic regions: the particle size is much smaller than the wavelength, the particle size is comparable to the wavelength and the particle size is much larger than the wavelength. Rayleigh scattering and geometric optics are applicable to the first and third regions respectively. Our research work is focused on the second region where the particle size is comparable to the wavelength and all the following discussions will be relevant to that region. The Mie method can be used for spherical particles, and the T-matrix[2], under certain limitations, can be used to calculate particles with rotational symmetry, however for irregular shapes or inhomogeneous particles, numerical methods are the only way to give accurate simulations. Besides the scattering process from an external source, dipole emission radiation as an internal source is another essential topic important for aerosol detection and remote-sensing technology. Numerical methods are again the only way to simulate the dipole emission process for irregular and inhomogeneous particles.

Besides radiative interaction with a single particle, radiative interactions with a medium consisting of large number of scatterers involve multiple scattering. In an atmosphere-ocean system, the radiation field not only depends on the atmosphere and ocean, but it also depends on the shape of the intervening ocean surface, where specular reflection and refraction govern the behavior.

The journal model is Optics Express.

The primary goal of this dissertation, as it was titled, focuses on two parts: the first part is to explore radiative interactions with single irregular particles by numerical simulation, which includes scattering and internal dipole emission; the second part focuses on radiative interactions in atmosphere-ocean system where multiple scattering and time dependent ocean surface are studied. Before we go into these two parts, we first introduce concepts, definitions and basic equations used in studying radiative interactions.

A. Radiative interactions with materials

How the radiation field interacts with materials? From the microscopic view, all materials are composed of molecules, atoms and even free electrons (as in metals), which are charged systems. The Electromagnetic field interacts with these charged micro systems in several ways:

- Electric charges in charged systems are driven to oscillate at the same frequency as the radiation source, oscillations of the charges will emit the same-frequency electromagnetic waves in all directions;

- Quantum states are changed by radiation field and the electromagnetic waves with a new frequency will be re-emitted.

The first kind of interaction includes all elastic scattering processes, and the second kind of interaction includes Raman scattering, fluorescence, etc. In both cases, part of the radiative source energy could be transformed to other forms of energy, such as thermal energy. In this dissertation, we focused on the first type of interaction, where only the elastic scattering is concerned. We also focus our interest on dielectric materials, where there is no contribution from free electrons.

Although the basic scattering scheme is at the molecular or atomic level on the charged micro-system, we are interested in particles with much larger size. Particles, such as dust and water droplets, consist of large number of molecules. For solid- or liquid-state material, the cumulative electromagnetic properties of these molecules are represented by the permittivity and permeability of the material. Our simulation and discussion also focused on materials with well defined permittivity and permeability values.

B.   Light polarization and scattering geometry

First of all, we introduce the quantity to describe the radiative strength – radiance. As shown in Fig. 1, ΔE is the energy of the radiance field that transfers across the small area $d\sigma$ in $\hat{s}$ direction, within solid angle $d\Omega$ and in frequency interval $(\nu,\nu+d\nu)$. The radiance (L) can be defined in the following equation:

$$\Delta E = L_\nu(\hat{s})cos\theta d\Omega d\sigma dt d\nu \tag{1.1}$$

In the following content of this dissertation, we only study single frequency radiative interactions. The dependence on frequency for radiance defined above will be omitted and we use L for radiance. Another important quantity is so called irradiance (I), which means the energy flux per unit area. A special property of radiance is that it is independent of the distance from the source. For instance, although the light irradiance of sunlight reaching earth is much smaller than the irradiance at the sun surface, their radiances are the same.

Both the electric field and magnetic field are vectors, besides the radiance and irradiance, polarization is another important parameter characterizing the property of light. As shown in Fig. 2, the incident beam and the scattered beam determine a
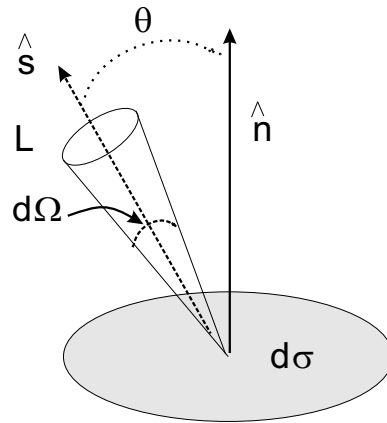
Fig. 1. Definition of radiance.

plane called the scattering plane, the electric field can be decomposed into parallel and perpendicular components relative to the scattering plane. We should note that the so-called "scattered" beam means the scattered field at a distance from the scattering object that is much larger than the wavelength of the electromagnetic wave. The radiative field at this distance can be treated locally as a spherically outward field.
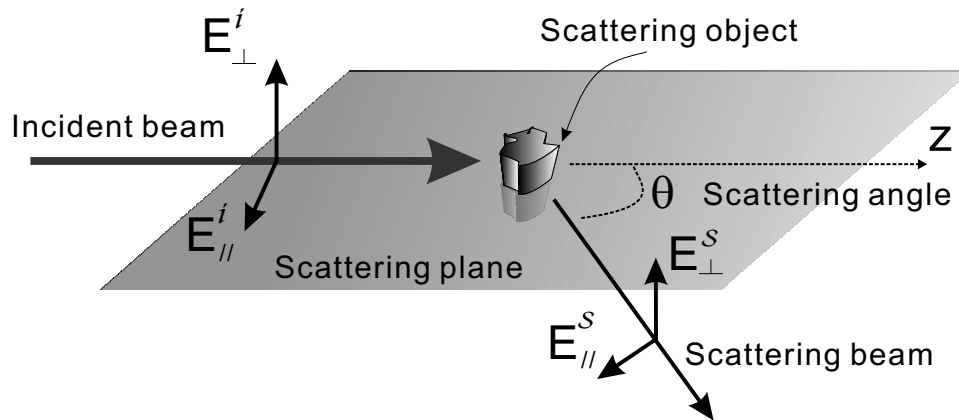
Fig. 2. Polarization and scattering geometry.

A transformation matrix connects the source and the scattered field:

$$
\begin{pmatrix} E_\parallel^s \\ E_\perp^s \end{pmatrix} = \frac{e^{-ikr-i\omega t}}{ikr} \begin{pmatrix} s_2 & s_3 \\ s_4 & s_1 \end{pmatrix} \begin{pmatrix} E_\parallel^i \\ E_\perp^i \end{pmatrix} \tag{1.2}
$$

The transformation matrix is called the scattering matrix or "Jone's matrix". Its elements s_j (j=1,2,3,4) depend not only on the properties of the scatterer itself, but also on the scattering angle θ and azimuthal angle ϕ. And in general, Jone's matrix elements are all complex numbers. There are seven independent parameters as well as a common phase parameter. Each optical instruments such as a lens or a polarizer has its own Jone's matrix, which is essential when considering coherence effects.

In general, the irradiance and polarization of a light beam is fully described by the Stoke's vector defined as:

$$
\begin{aligned}
I &= \left\langle E_\parallel E_\parallel^* + E_\perp E_\perp^* \right\rangle \\
Q &= \left\langle E_\parallel E_\parallel^* - E_\perp E_\perp^* \right\rangle \\
U &= \left\langle E_\parallel E_\perp^* + E_\perp E_\parallel^* \right\rangle \\
V &= i \left\langle E_\parallel E_\perp^* - E_\perp E_\parallel^* \right\rangle
\end{aligned} \tag{1.3}
$$

where an asterisk denotes the complex conjugate complex value, and $< \cdots >$ denotes the temporal average. Since the Stoke's vector elements are all real numbers, there is a 4×4 transformation matrix connecting the incident and scattered light. Stokes vector also depends on the reference plane. If the reference plane is the scattering plane shown in Fig. 2, the transformation matrix is:

$$
\begin{pmatrix} I_s \\ Q_s \\ U_s \\ V_s \end{pmatrix} = \frac{1}{k^2 r^2} \begin{pmatrix} P_{11} & P_{12} & P_{13} & P_{14} \\ P_{21} & P_{22} & P_{23} & P_{24} \\ P_{31} & P_{32} & P_{33} & P_{34} \\ P_{41} & P_{42} & P_{43} & P_{44} \end{pmatrix} \begin{pmatrix} I_i \\ Q_i \\ U_i \\ V_i \end{pmatrix} \tag{1.4}
$$

where $k = 2\pi/\lambda$, and λ is the wavelength. The matrix $(P_{i,j}, \; i,j = 1,2,3,4)$ are called the phase matrix, and the first element P_{11} is called the phase function. If the reference plane is chosen by a fixed plane in space, the transformation matrix defined below is called the Mueller matrix:

$$\begin{pmatrix} I_s \\ Q_s \\ U_s \\ V_s \end{pmatrix} = \frac{1}{k^2 r^2} \begin{pmatrix} m_{11} & m_{12} & m_{13} & m_{14} \\ m_{21} & m_{22} & m_{23} & m_{24} \\ m_{31} & m_{32} & m_{33} & m_{34} \\ m_{41} & m_{42} & m_{43} & m_{44} \end{pmatrix} \begin{pmatrix} I_i \\ Q_i \\ U_i \\ V_i \end{pmatrix} \tag{1.5}$$

Since the only difference between phase matrix and Mueller matrix is their reference planes, a rotation operation can transform one to the other.

We also need to note that although phase matrix (or Mueller matrix) can be derived from scattering matrix for a single particle, so the total independent numbers of the single particle phase matrix is same as the scattering matrix, which is however not true for the multiple scattering case. In general for multiple scattering medium, the phase matrix has 16 independent elements, which is due to the incoherent scattering by multiple scatterers in the medium. In reality, for multiple scattering study of turbid medium containing scatterers, the symmetry of the scatterer and the random orientation condition would greatly simplify the phase matrix as shown in [3].

Both scattering and absorption will take energy from the initial source direction. For scattering, the the total redirected power divided by the illuminating irradiance is defined as the scattering cross section σ_s. Similarly, σ_a is absorption cross section. Their summation, $\sigma_e = \sigma_s + \sigma_a$, is called the extinction cross section. The ratio of scattering cross section to the extinction cross section is called scattering albedo ω_0.

C. Radiative transfer equation

In general, a medium, such as an atmosphere, not only contains scatterers, it also contains absorbers and emitters. If we assume these optical effects are independent from particle to particle and the radiation field is static, an equation called the Radiative Transfer Equation [4] completely describes the radiation field in this medium.

$$-\frac{1}{\kappa}(\hat{\mathbf{s}} \cdot \nabla)L(\mathbf{r},\hat{\mathbf{s}}) = L(\mathbf{r},\hat{\mathbf{s}}) - \omega_0 \int p(\mathbf{s},\hat{\mathbf{s}}')L(\mathbf{r},\hat{\mathbf{s}}')d\Omega' + j_v(\hat{\mathbf{s}}) \qquad (1.6)$$

where κ is the extinction coefficient (in unit of $length^{-1}$), L is the radiance defined earlier, p is the phase function, ω_0 is the single scattering albedo, and j_v corresponds to the source (emitters). In our research, we are interested in visible light and the source term will be ignored. Knowing the scatterer's density ρ, the extinction can be calculated as: $\kappa = \sigma_e \rho$.

We also note that the radiation field in a medium is a vector field. As we discussed earlier, radiance itself can not characterize the radiation field completely. To get the correct equation for radiative transfer for a vector field, Eq. 1.6 needs to be modified: Radiance L will be replaced by a vector related to Stokes vector, and the phase matrix is replaced by the Mueller matrix. Solving the radiative equation is not a major concern in this dissertation; however we will show the differences between the scale field and the vector field in chapter VIII.

CHAPTER II

FINITE-DIFFERENCE TIME-DOMAIN METHOD

In the 19th century, both experimental and theoretical studies on magnetic and electric fields have made great breakthroughs. Ampere's law, Faraday's law and Gauss's law were found one by one. James Clerk Maxwell added a term called displacement current and finally wrote down the complete equations which fully describe the behavior of electric and magnetic fields. These equations are named Maxwell's equations. After that, solving Maxwell's equations for different conditions has always been an important and fruitful research field. In the past, solving Maxwell's equations in the frequency domain attracted most of the attention. The method based on the frequency domain met with great difficulty in solving complex systems with irregular shape of boundaries and heterogenous dielectric properties. With the invention of digital computers and its rapid development, solving Maxwell's equations in the time domain now becomes possible. Yee introduced the finite-difference time-domain (FDTD) method in 1966 [5], which is a powerful approach to numerically solving Maxwell's equations in the time domain. FDTD has many advantages in that it can solve Maxwell's equations for complex dielectric systems if the optical properties (such as refractive index) are known for the system. Many theoretical efforts have been carried out to enhance this method [6]. With the advances in computer science and technology that brought powerful computer facilities, the FDTD method has been successfully applied to solve problems in many disciplines. In this chapter, we will give a brief introduction of FDTD.

A.   Maxwell's equations and FDTD

One of the formulations of Maxwell's equations is:

$$\nabla \cdot D = \rho$$

$$\nabla \cdot B = 0$$

$$\nabla \times \mathbf{H} = \frac{\partial \mathbf{D}}{\partial t} + \vec{j}$$

$$\nabla \times \mathbf{E} = -\frac{\partial \mathbf{B}}{\partial t}$$

(2.1)

where $\mathbf{E}$ is electric field, $\mathbf{D}$ is electric displacement, $\mathbf{B}$ is magnetic flux density, $\mathbf{H}$ is magnetic field, j is electric current density and ρ is free electric charge density. $\mathbf{E}$ and $\mathbf{D}$ are related by $\mathbf{D} = \epsilon_r \epsilon_0 \mathbf{E}$, where ϵ_0 is the vacuum electrical permittivity and ϵ_r is the relative permittivity. $\mathbf{B}$ and $\mathbf{H}$ are related by $\mathbf{B} = \mu_r \mu_0 \mathbf{H}$, where μ_0 is the vacuum magnetic permeability and μ_r is the relative permeability. We also need to note that the speed of light in vacuum is $c = 1/\sqrt{\epsilon_0 \mu_0}$.

FDTD use only the last two curl equations of Maxwell's equations, that is:

$$\nabla \times \mathbf{H} = \frac{\partial \mathbf{D}}{\partial t} + \vec{j}$$

$$\nabla \times \mathbf{E} = -\frac{\partial \mathbf{B}}{\partial t}$$

(2.2)

One question arises now as to why FDTD only needs two of the four Maxwell's equations? The answer is that in FDTD, we solve the equations in the time domain, if the initial condition is satisfied the two divergence equations, then these equations will be satisfied throughout the entire simulation. For example, if we take the divergence of both sides of the second curl equation, since $\nabla \cdot (\nabla \times \mathbf{A}) = 0$ is valid for any vector $\mathbf{A}$, the second curl equation in Eq. 2.2 becomes:

$$\frac{\partial (\nabla \cdot \mathbf{B})}{\partial t} = 0$$

(2.3)

which means that $\nabla \cdot \mathbf{B}$ is a constant. If at the initial time of the simulation, we set $\nabla \cdot \mathbf{B} = 0$ (such as $\mathbf{B}|_{t=0} = 0$), then this relation will be hold through the entire simulation process. Divergenceless of $\mathbf{B}$ is satisfied in the FDTD. A similar derivation can be used to show that Gauss's law is also satisfied in FDTD if the initial conditions are chosen correctly.

Although in general any material except a vacuum is dispersive, which means that the refractive index depends on the electromagnetic wave frequency. Our interest is on the single frequency response or nearly non-dispersive medium, thus we assume ϵ_r and μ_r are time independent. Further more, we also assume that the relative magnetic permeability is unity since all materials we are interested in are nonmagnetic. For computational convenience, we used new field values defined as $\mathbf{E} = \sqrt{\mu_0/\epsilon_0}\mathbf{E}'$. Substituting E' back into Eq. 2.2, and after some simple mathematic rearrangement, we obtain:

$$
\begin{aligned}
\nabla \times \mathbf{H} &= \frac{\epsilon_r}{c}\frac{\partial \mathbf{E}'}{\partial t} + \vec{j} \\
\nabla \times \mathbf{E}' &= -\frac{1}{c}\frac{\partial \mathbf{H}}{\partial t}
\end{aligned}
\tag{2.4}
$$

In the rest of the dissertation, we will use Eq. 2.4 to do FDTD simulation, and we will omit the superscript symbol from $\mathbf{E}'$.

B.   A one dimensional FDTD example

A simple one dimensional FDTD example will demonstrate how FDTD works. We want to simulate a Gaussian wave pulse generated in vacuum, and let it transport along the z direction pasing a region having different refractive index. As shown in Fig. 3, the electric field is parallel to the x-axis and the magnetic field is parallel to the y-axis. It is worthy noting that in FDTD the electric field and the magnetic field are no longer in the same spatial position. If we number the position of the electric

field as "0,1,2...,12", the magnetic field's position is "0.5,1.5,...11.5". The grid length is denoted as Δz. The one dimensional space is not homogenous, there is one shaded region having relative refractive index m=1.5. The relation between refractive index and permeability is $m = \sqrt{\epsilon_r}$. Outside the shaded region is vacuum, whose relative refractive index is 1. The Gaussian pulse is generated at position z=3.
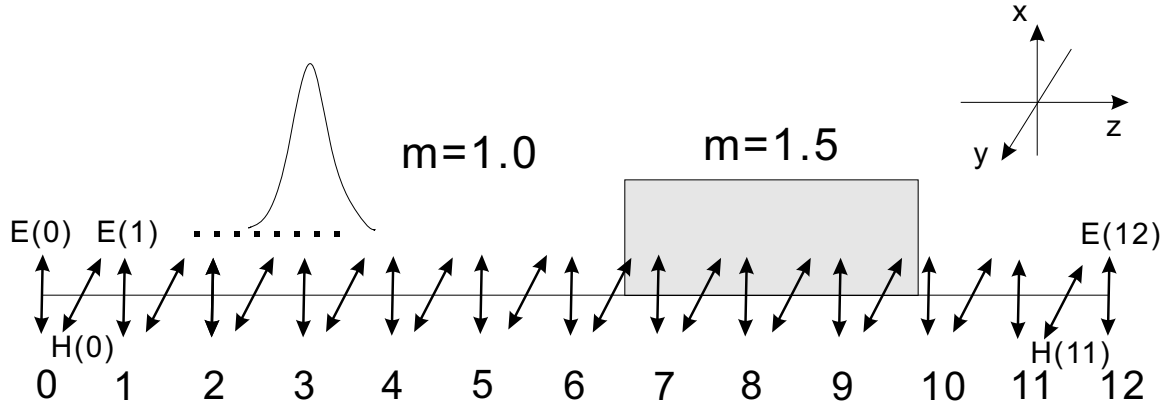
Fig. 3. An example of one dimensional FDTD model.

According to Eq. 2.4, FDTD formula for one dimensional case is:

$$-\frac{\partial H_y}{\partial z} = \frac{\epsilon_r}{c}\frac{\partial E_x}{\partial t}$$
$$\frac{\partial E_x}{\partial z} = -\frac{1}{c}\frac{\partial H_y}{\partial t} \tag{2.5}$$

We used second order leapfrog algorithm to discretize both the spatial and temporal derivatives.

$$\frac{\partial H_y^{m+1/2}(z)}{\partial z}\Big|_{z=n} \doteq \frac{H_y^{m+1/2}(n+1/2) - H_y^{m+1/2}(n-1/2)}{\Delta z},$$
$$\frac{\partial H_y^t(n+1/2)}{\partial t}\Big|_{t=m} \doteq \frac{H_y^{m+1/2}(n+1/2) - H_y^{m-1/2}(n+1/2)}{\Delta t},$$
$$\frac{\partial E_x^m(z)}{\partial z}\Big|_{z=n+1/2} \doteq \frac{E_x^m(n+1) - E_x^m(n)}{\Delta z}, \tag{2.6}$$
$$\frac{\partial E_x^t(n)}{\partial t}\Big|_{t=m+1/2} \doteq \frac{E_x^{m+1}(n) - E_x^m(n)}{\Delta t}$$

where $H_y^{m+1/2}(n+1/2)$ represents the magnetic field at the spatial position $z = (n+1/2)\Delta z$ and at time $t = (m+1/2)\Delta t$. Same notations are used in the electric field representation.

Except the two end points E(0) and E(12), substituting Eq. 2.6 into Eq. 2.5, the temporal updating terms can be obtained:

$$E_x^{m+1}(n) = E_x^m(n) - \frac{1}{\epsilon_r(n)} \frac{c\Delta t}{\Delta z} \left[H_y^{m+1/2}(n+1/2) - H_y^{m+1/2}(n-1/2) \right]$$

$$H_y^{m+3/2}(n+1/2) = H_y^{m+1/2}(n+1/2)$$
$$- \frac{c\Delta t}{\Delta z} \left[\epsilon_r(n+1)E_x^{m+1}(n+1) - \epsilon_r(n)E_x^{m+1}(n) \right]$$

$$(2.7)$$

Gaussian pulse source is added into the model as:

$$E_x^{m+1}(n) = E_x^{m+1}(n) + e^{-(n-T_0)^2/w^2} \tag{2.8}$$

where T_0 is a preset integer corresponding to the maximum of the pulse. w is another factor to control the width of the pulse.

Even the simplest one dimensional case as shown in Fig. 3, the line can't be elongated to infinity in either direction. The points at the two ends need to be carefully treated since we can not apply the formula used in Eq. 2.7 to do temporal updating. It is well known that the speed of light c is a constant in free space, which is independent of frequency and direction. A very simple but reflectionless boundary condition especially for the one dimensional case can be obtained as follows: Firstly, special spatial intervals and temporal intervals are set to satisfy $c\Delta t/\Delta z = 1/2$, whose physical meaning is that the light need $2\Delta t$ temporal intervals to pass one spatial grid distance; then in coding, $E^{n+2}(0) = E^n(1)$ and $E^{n+2}(12) = E^n(11)$ are used to update electric field values at two ends. This boundary can be easily achieved in the computing code which is in the Appendix A. The absorbing boundary condition

(ABC) used in one dimensional FDTD shown here can not be applied to higher dimension conditions, and we will discuss it later in this chapter.

C. Numerical dispersion and stability

All numerical methods to simulate wave propagation unavoidably face two concerns: numerical dispersion and numerical stability.

1.   Numerical dispersion

Wave propagating in discretized space and time is different from that when it travels in continuous space-time. Numerical dispersion is one of the intrinsic properties resulting from the discretization. Assume the numerical wave in one dimensional free space is:

$$\mathbf{E}_x^m(n) = \hat{x}E_0 e^{i\tilde{k}_z n\Delta z - i\omega m\Delta t},$$

$$\mathbf{H}_y^{m+1/2}(n+1/2) = \hat{y}E_0 e^{i\tilde{k}_z(n+1/2)\Delta z - i\omega(m+1/2)\Delta t}$$

$$(2.9)$$

where $\tilde{k}$ is the numerical wave number ($k = 2\pi/\lambda$, λ is the wavelength) in simulation.

Substituting the numerical wave form above into Eq. 2.7, and factoring out common factor $e^{i\tilde{k}_z n\Delta z - i\omega m\Delta t}$, we can obtain:

$$E_0 e^{-i\omega\Delta t} = E_0 - \frac{c\Delta t}{\Delta z}H_0\left[e^{i\tilde{k}_z\Delta z/2 - i\omega\Delta t/2} - e^{-i\tilde{k}_z\Delta z/2 - i\omega\Delta t/2}\right]$$

$$H_0 e^{-i\omega\Delta t} = H_0 - \frac{c\Delta t}{\Delta z}E_0\left[e^{i\tilde{k}_z\Delta z/2 - i\omega\Delta t/2} - e^{-i\tilde{k}_z\Delta z/2 - i\omega\Delta t/2}\right]$$

$$(2.10)$$

Substituting one field into another, and after some mathematical transforms, numerical wave vector is obtained as:

$$\tilde{k}_z = \frac{2}{\Delta z}sin^{-1}\left(\frac{\Delta z}{c\Delta t}sin(\frac{\omega\Delta t}{2})\right)$$

In the general case, numerical wave vector $\tilde{k}_z$ is not equal to real wave vector. In

the limit $\Delta z \to 0$ and $\Delta t \to 0$, we have $\tilde{k}_z \to k_z$. It is worthy to note that there is a "magic time step" to avoid the numerical dispersion if we use $c\Delta t = \Delta z$. Although the numerical solution will be exact for one dimensional FDTD, a similar "magic time step" can be found in higher dimensional FDTD, this has little practical application since it is only satisfied along the specifically fixed transmission direction which is hard to satisfy in 2D or 3D simulations.

2.   Numerical stability

We also need to note that the spatial and temporal increments can not be chosen arbitrarily otherwise the simulation will be unstable. These parameters must satisfy the so called Courant-Friedrichs-Levy (CFL) condition[6] in the form: $c\Delta t \leq \Delta z$. In 2D and 3D FDTD formulas, the CFL condition will be different as:

$$
\begin{aligned}
c\Delta t &\leq \frac{1}{\sqrt{\frac{1}{\Delta x^2} + \frac{1}{\Delta y^2}}} \quad (2D) \\
c\Delta t &\leq \frac{1}{\sqrt{\frac{1}{\Delta x^2} + \frac{1}{\Delta y^2} + \frac{1}{\Delta z^2}}} \quad (3D)
\end{aligned}
\tag{2.11}
$$

D.   Three dimensional FDTD formula

Although many basic ideas of FDTD have been introduced previously in a one dimensional example, real world models are mostly three-dimensional, and three-dimensional FDTD has many differences when compared with the one-dimensional case. In this section, we will describe the FDTD grid setup, field updating, and absorbing boundary condition in 3D FDTD.

1.   FDTD grid set up

In most general case of 3D model, both electric and magnetic fields have three components:E_x, E_y, E_z, H_x, H_y and H_z. Similar to the one dimensional case, electric and magnetic fields are spatially displaced. Our FDTD formulation uses the common cube grid cells as shown in Fig. 4, electric fields are placed at the center of the edge with the direction along the edge on which they are located, and magnetic fields are placed in the center of the six faces with their directions along the outward normals of their respective surfaces. Our FDTD set the coordinates so that the center of this cube is (I,J,K).
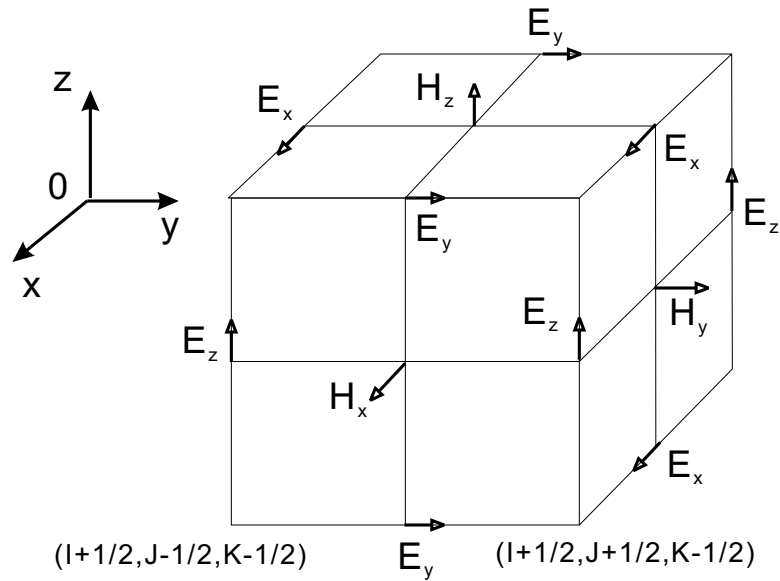
Fig. 4. Three dimensional FDTD grid.

2.   Field updating in time domain

Compared with the one dimensional FDTD formulation, the 3D formulation would be much more complicated, we first give the general expression of the field updating

in the computation region.

$$E_x^{n+1}\left(I, J+\frac{1}{2}, K+\frac{1}{2}\right)$$

$$= a\left(I, J+\frac{1}{2}, K+\frac{1}{2}\right) E_x^n\left(I, J+\frac{1}{2}, K+\frac{1}{2}\right) + b\left(I, J+\frac{1}{2}, K+\frac{1}{2}\right)$$

$$\times \left\{ \frac{c\Delta t}{\Delta y}\left[H_z^{n+1/2}\left(I, J+1, K+\frac{1}{2}\right) - H_z^{n+1/2}\left(I, J, K+\frac{1}{2}\right)\right]\right.$$

$$\left. + \frac{c\Delta t}{\Delta z}\left[H_z^{n+1/2}\left(I, J+\frac{1}{2}, K\right) - H_z^{n+1/2}\left(I, J+\frac{1}{2}, K+1\right)\right]\right\} \qquad (2.12)$$

$$E_y^{n+1}\left(I+\frac{1}{2}, J, K+\frac{1}{2}\right)$$

$$= a\left(I+\frac{1}{2}, J, K+\frac{1}{2}\right) E_y^n\left(I+\frac{1}{2}, J, K+\frac{1}{2}\right) + b\left(I+\frac{1}{2}, J, K+\frac{1}{2}\right)$$

$$\times \left\{ \frac{c\Delta t}{\Delta x}\left[H_z^{n+1/2}\left(I, J, K+\frac{1}{2}\right) - H_z^{n+1/2}\left(I+1, J, K+\frac{1}{2}\right)\right]\right.$$

$$\left. + \frac{c\Delta t}{\Delta z}\left[H_x^{n+1/2}\left(I+\frac{1}{2}, J, K+1\right) - H_x^{n+1/2}\left(I+\frac{1}{2}, J, K\right)\right]\right\} \qquad (2.13)$$

$$E_z^{n+1}\left(I+\frac{1}{2}, J+\frac{1}{2}, K\right)$$

$$= a\left(I+\frac{1}{2}, J+\frac{1}{2}, K\right) E_z^n\left(I+\frac{1}{2}, J+\frac{1}{2}, K\right) + b\left(I+\frac{1}{2}, J+\frac{1}{2}, K\right)$$

$$\times \left\{ \frac{c\Delta t}{\Delta y}\left[H_x^{n+1/2}\left(I+\frac{1}{2}, J, K\right) - H_x^{n+1/2}\left(I+\frac{1}{2}, J+1, K\right)\right]\right.$$

$$\left. + \frac{c\Delta t}{\Delta x}\left[H_y^{n+1/2}\left(I+1, J+\frac{1}{2}, K\right) - H_y^{n+1/2}\left(I, J+\frac{1}{2}, K\right)\right]\right\} \qquad (2.14)$$

and the magnetic field updating formula:

$$
H_x^{n+1/2}\left(I+\frac{1}{2}, J, K\right)
$$

$$
= H_x^{n-1/2}\left(I+\frac{1}{2}, J, K\right)
$$

$$
+ \left\{\frac{c\Delta t}{\Delta y}\left[E_z^n\left(I+\frac{1}{2}, J-\frac{1}{2}, K\right) - E_z^n\left(I+\frac{1}{2}, J+\frac{1}{2}, K\right)\right]\right.
$$

$$
\left. + \frac{c\Delta t}{\Delta z}\left[E_y^n\left(I+\frac{1}{2}, J, K+\frac{1}{2}\right) - E_y^n\left(I+\frac{1}{2}, J, K-\frac{1}{2}\right)\right]\right\} \qquad (2.15)
$$

$$
H_y^{n+1/2}\left(I, J+\frac{1}{2}, K\right)
$$

$$
= H_y^{n-1/2}\left(I, J+\frac{1}{2}, K\right)
$$

$$
+ \left\{\frac{c\Delta t}{\Delta z}\left[E_x^n\left(I, J+\frac{1}{2}, K-\frac{1}{2}\right) - E_x^n\left(I, J+\frac{1}{2}, K+\frac{1}{2}\right)\right]\right.
$$

$$
\left. + \frac{c\Delta t}{\Delta x}\left[E_z^n\left(I+\frac{1}{2}, J+\frac{1}{2}, K\right) - E_z^n\left(I-\frac{1}{2}, J+\frac{1}{2}, K\right)\right]\right\} \qquad (2.16)
$$

$$
H_y^{n+1/2}\left(I, J+\frac{1}{2}, K\right)
$$

$$
= H_y^{n-1/2}\left(I, J+\frac{1}{2}, K\right)
$$

$$
+ \left\{\frac{c\Delta t}{\Delta z}\left[E_x^n\left(I, J+\frac{1}{2}, K-\frac{1}{2}\right) - E_x^n\left(I, J+\frac{1}{2}, K+\frac{1}{2}\right)\right]\right.
$$

$$
\left. + \frac{c\Delta t}{\Delta x}\left[E_z^n\left(I+\frac{1}{2}, J+\frac{1}{2}, K\right) - E_z^n\left(I-\frac{1}{2}, J+\frac{1}{2}, K\right)\right]\right\} \qquad (2.17)
$$

$$H_z^{n+1/2}\left(I, J, K + \frac{1}{2}\right)$$

$$= H_z^{n-1/2}\left(I, J, K + \frac{1}{2}\right)$$

$$\times \left\{ \frac{c\Delta t}{\Delta x} \left[E_y^n\left(I - \frac{1}{2}, J, K + \frac{1}{2}\right) - E_y^n\left(I + \frac{1}{2}, J, K + \frac{1}{2}\right) \right] \right.$$

$$\left. + \frac{c\Delta t}{\Delta y} \left[E_x^n\left(I, J + \frac{1}{2}, K + \frac{1}{2}\right) - E_x^n\left(I, J - \frac{1}{2}, K + \frac{1}{2}\right) \right] \right\} \quad (2.18)$$

a and b coefficients in electric field updating terms are related to the local permittivity. There are several schemes to determine their values [1], we present our scheme in Appendix B.

3. Total-Field/Scattered-Field

In our FDTD code, we also take advantage of Total-Field/Scattered-Field technique [7, 8]. Because of the linearity of Maxwell's equations, both electric and magnetic fields can be decomposed into incident and scattered components:

$$\mathbf{E}_{total} = \mathbf{E}_{inc} + \mathbf{E}_{scat}, \quad \mathbf{H}_{total} = \mathbf{H}_{inc} + \mathbf{H}_{scat} \quad (2.19)$$

where $\mathbf{E}_{inc}$ and $\mathbf{H}_{inc}$ are known external source, $\mathbf{E}_{scat}$ and $\mathbf{H}_{scat}$ are unknown fields we want to obtain. As shown in Fig. 5, a virtual surface separates region 1 and region 2. In region 1, total fields are simulated, in region 2, only scattered fields are simulated. Separating the total field and the scattered field has many advantages such as easy coding for arbitrary source condition; less errors from the reflection by simulation boundary, etc.

To demonstrate how to implement this technique, we use a 2D FDTD model as shown in Fig. 6 and we also assume that the spatial region shown in the figure is

FDTD Simulation Region
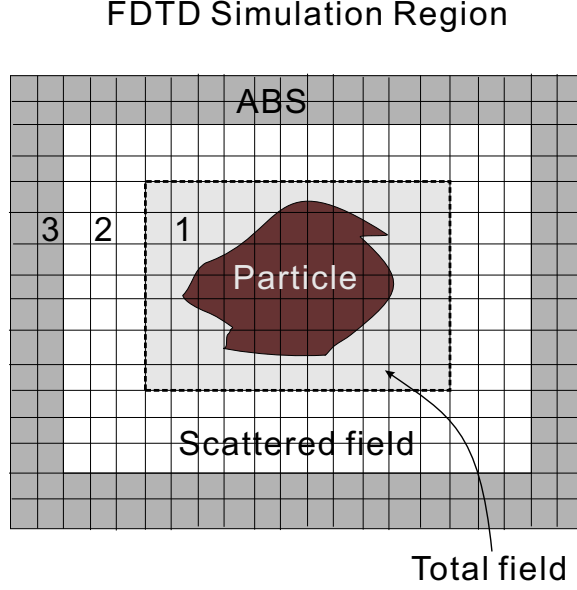
Fig. 5. FDTD simulation region.

vacuum. For a 2D TE_z mode FDTD, Maxwell's equations in vacuum are:

$$\frac{\partial H_z}{\partial y} = \frac{1}{c}\frac{\partial E_x}{\partial t}$$
$$-\frac{\partial H_z}{\partial x} = \frac{1}{c}\frac{\partial E_y}{\partial t} \qquad (2.20)$$
$$\frac{\partial E_y}{\partial x} - \frac{\partial E_x}{\partial y} = -\frac{1}{c}\frac{\partial H_z}{\partial t}$$

Assuming that the source fields E_{inc} and H_{inc} are known. If we want to temporally update $E_x(I, J - 1/2)$, which is in the total field region, we should use the formula:

$$E_x^{n+1}(I, J - 1/2) = E_x^n(I, J - 1/2) + \frac{c\Delta t}{\Delta y}\left[H_z^{n+1/2}(I, J) - H_z^{n+1/2}(I, J - 1)\right] \quad (2.21)$$

Because the position (I,J-1) lies in the scattering field region, the $H_z(I, J - 1)$ value used in the FDTD code only represents the scattered field. Thus the above equation itself is not enough for temporal updating because we missed the source field's contribution. Since the incident field is known, this inconsistency can be solved by

adding another operation after the operation in Eq. 2.21 to compensate for the source contribution in the electric field updating:

$$E_x^{n+1}(I, J-1/2) = E_x^{n+1}(I, J-1/2) - \frac{c\Delta t}{\Delta y} H_{inc}^{n+1/2}(I, J-1) \qquad (2.22)$$

Similar compensation operation is also needed for temporal updating of $H_z(I, J-1)$.

In 3D FDTD, more complication of the system's structure increases, more field values along the 2D cross section at any cutting surface are needed to undergo the compensation operations; however we will not give the detailed results.
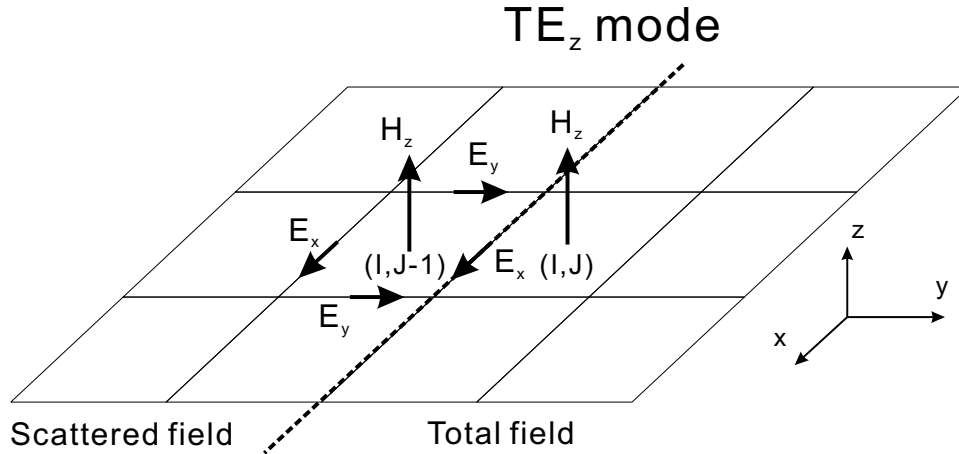
Fig. 6. Total-Field/Scattered-Field technique in a 2D model.

E.   Absorbing boundary condition

If the simulated electromagnetic field is limited in a region, such as the simulation of the EM field inside a cavity with a perfect conductor boundary, one just forces the electric field values at the boundary to be zero, and the simulation can proceed.

In many other cases, we need to study the simulation of the EM field going into an unbounded region, such as the scattering by particles, underground mine detection

and radar design, etc. Since any computer can only store data in a limited region, artificial boundary conditions are required. Many researchers have been searching for suitable absorbing boundary conditions in the past two decades. In 1994, Perfect Matched Layer (PML) boundary condition was developed by Berenger [9], and later on in 1995 Uniaxial Perfect Matched Layer (UPML) was also put forward by Sacks et al. [10]. Theoretically, PML and UPML can absorb any radiation no matter what the frequency or direction onto the boundary without reflection. In this section, we will introduce basic ideas of UPML boundary condition which is used in our FDTD code.

We first examine a simple case, as shown in Fig. 7. The space is divided into two regions: x<0 and x>0. We assume region 1 is homogenous but region 2 has uniaxial anisotropy with rotational symmetry about the x-axis, the permittivity and permeability of the uniaxial medium are:

$$\bar{\bar{\epsilon}}_2 = \epsilon_2 \begin{pmatrix} a & 0 & 0 \\ 0 & b & 0 \\ 0 & 0 & b \end{pmatrix}, \quad \bar{\bar{\mu}}_2 = \mu_2 \begin{pmatrix} c & 0 & 0 \\ 0 & d & 0 \\ 0 & 0 & d \end{pmatrix} \tag{2.23}$$

As shown in Fig. 7, a plane parallel wave $\mathbf{H}^{in} = \mathbf{H}_0 e^{i\mathbf{k}_1 \cdot \mathbf{r}}$ is illuminating on the surface $x = 0$, where $\mathbf{k}$ is wave vector which is defined as the direction of the wave propagation with the magnitude of the wave number. Without loss of generality, we assume the z-component of the wave vector is zero. Then $\mathbf{k}_1 = \hat{x}k_{x1} + \hat{y}k_{y1}$. The transmitted field in region 2 is also a plane wave without a z-component in the wave vector. From Maxwell's curl equations:

$$\nabla \times \mathbf{H}_2 = \frac{\partial \mathbf{D}_2}{\partial t}, \ i\mathbf{k}_2 \times \mathbf{H}_2 = -i\omega\bar{\bar{\epsilon}}_2\mathbf{E}_2$$
$$\nabla \times \mathbf{E}_2 = -\frac{\partial \mathbf{B}_2}{\partial t}, \ i\mathbf{k}_2 \times \mathbf{E}_2 = i\omega\bar{\bar{\mu}}_2\mathbf{H}_2 \tag{2.24}$$

the wave functions for $\mathbf{H}$ (H_x, H_y, H_z) can be derived:

$$\mathbf{k}_2 \times (\bar{\bar{\epsilon}}_2^{-1} \mathbf{k}_2 \times \mathbf{H}) + \omega^2 \bar{\bar{\mu}}_2 \mathbf{H} = 0$$

Since $\mathbf{H}$ is a vector having three components, a matrix form can be obtained:

$$\begin{pmatrix} k_2^2 c - k_{2y}^2 b^{-1} & k_{2x} k_{2y} b^{-1} & 0 \\ k_{2x} k_{2y} b^{-1} & k_2^2 d - k_{2x}^2 b^{-1} & 0 \\ 0 & 0 & k_2^2 d - k_{2x}^2 b^{-1} - k_{2y}^2 a^{-1} \end{pmatrix} \begin{pmatrix} H_x \\ H_y \\ H_z \end{pmatrix} = 0 \qquad (2.25)$$

The determinant of the matrix above should be zero, which gives the following two equations:

$$\begin{aligned} k_2^2 - k_{2x}^2 b^{-1} d^{-1} - k_{2y}^2 a^{-1} d^{-1} = 0 & \quad : TE_z \ (H_x, H_y = 0) \\ k_2^2 - k_{2x}^2 b^{-1} d^{-1} - k_{2y}^2 b^{-1} c^{-1} = 0 & \quad : TM_z \ (H_z = 0) \end{aligned} \qquad (2.26)$$

From the boundary condition at $x = 0$, one can now calculate the reflection and transmission coefficients for light shinning from region 1 to region 2. Assuming Γ and τ are reflection and transmission coefficients respectively, the waves in region 1 and region 2 are:

$$\begin{aligned} \mathbf{H}_1 &= \hat{z} H_0 (1 + \Gamma e^{-2i k_{1x} x}) e^{i(k_{1x} x + k_{1y} y)} \\ \mathbf{E}_1 &= i \frac{1}{\omega \epsilon_1} \nabla \times \mathbf{H}_1 \\ &= \left[-\hat{x} \frac{k_{1y}}{\omega \epsilon_1} (1 + \Gamma e^{-2i k_{1x} x}) + \hat{y} \frac{k_{1x}}{\omega \epsilon_1} (1 - \Gamma e^{-2i k_{1x} x}) \right] H_0 e^{i(k_{1x} x + k_{1y} y)} \end{aligned} \qquad (2.27)$$
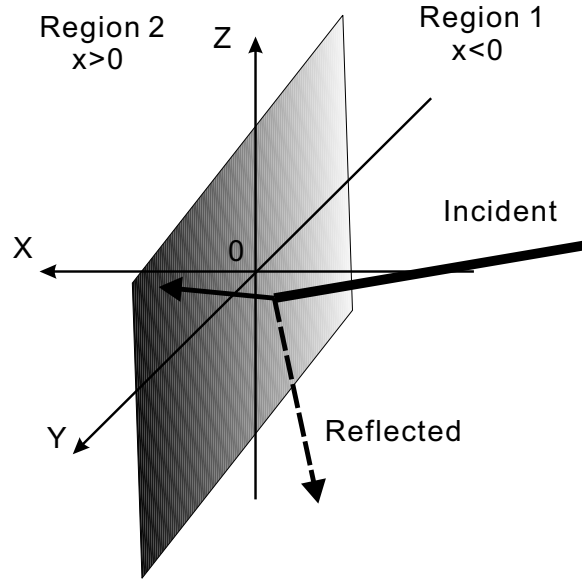
Fig. 7. An example of reflectionless layer.

For transmitted light within region 2, similar expressions are derived as:

$$\mathbf{H}_2 = \hat{z} H_0 \tau e^{i(k_{2x}x + k_{2y}y)}$$

$$\mathbf{E}_2 = \frac{i \bar{\bar{\epsilon}}_2^{-1}}{\omega} \nabla \times \mathbf{H}_2 \tag{2.28}$$

$$= \left[-\hat{x} \frac{k_{2y}}{\omega \epsilon_2 a} + \hat{y} \frac{k_{2x}}{\omega \epsilon_2 b} \right] H_0 \tau e^{i(k_{2x}x + k_{2y}y)}$$

Boundary condition requires that the tangential components of both $\mathbf{E}$ and $\mathbf{H}$ field along x=0 surface are continuous. From the equations obtained above, the continuity condition gives:

$$k_{2y} = k_{1y} \tag{2.29}$$

$$1 + \Gamma = \tau \tag{2.30}$$

$$\frac{k_{1x}}{\omega \epsilon_1}(1 - \Gamma) = \frac{k_{2x}}{\omega \epsilon_2 b} \tau \tag{2.31}$$

Then the reflection and transmission coefficients of magnetic field can be calculated:

$$\Gamma = \frac{k_{1x} - k_{2x}b^{-1}}{k_{1x} + k_{2x}b^{-1}}; \quad \tau = \frac{k_{1x}}{k_{1x} + k_{2x}b^{-1}} \tag{2.32}$$

According to the first equation of Eq. 2.26:

$$k_{2x} = \sqrt{k_2^2 bd - k_{1y}^2 a^{-1}b} \tag{2.33}$$

Since ϵ_2, μ_2, a, b and d are parameters to be set, to make the reflection coefficient zero for all k_{1x}, a set can be found as: $\epsilon_1 = \epsilon_2$, $\mu_1 = \mu_2$, $a^{-1} = b$ and $b = d$. Then we have $k_2 = k_1$, and:

$$k_{2x} = \sqrt{k_1^2 b^2 - k_{1y}^2 b^2} = k_{1x}b \tag{2.34}$$

Γ will be zero for all k_{1x} and all frequencies.

In case of TM_z mode, similar relations can be derived. Electric and Magnetic fields in region 1 are:

$$\mathbf{E}_1 = \hat{z}E_0(1 + \Gamma e^{-2ik_{1x}x})e^{i(k_{1x}x+k_{1y}y)}$$

$$\mathbf{H}_1 = -i\frac{1}{\omega\mu_1}\nabla \times \mathbf{E}_1 \tag{2.35}$$

$$= \left[\hat{x}\frac{k_{1y}}{\omega\mu_1}(1 + \Gamma e^{-2ik_{1x}x}) - \hat{y}\frac{k_{1x}}{\omega\mu_1}(1 - \Gamma e^{-2ik_{1x}x})\right]E_0 e^{i(k_{1x}x+k_{1y}y)}$$

and the transmitted fields within region 2 are:

$$\mathbf{E}_2 = \hat{z}E_0\tau e^{i(k_{2x}x+k_{2y}y)}$$

$$\mathbf{H}_2 = -\frac{i\bar{\bar{\mu}}_2^{-1}}{\omega}\nabla \times \mathbf{E}_2 \tag{2.36}$$

$$= \left[\hat{x}\frac{k_{2y}}{\omega\mu_2 c} - \hat{y}\frac{k_{2x}}{\omega\mu_2 d}\right]E_0\tau e^{i(k_{2x}x+k_{2y}y)}$$

From the same boundary condition at $x = 0$, one can obtain:

$$k_{2y} = k_{1y}$$

$$1 + \Gamma = \tau \tag{2.37}$$

$$\frac{k_{1x}}{\omega \mu_1}(1 - \Gamma) = \frac{k_{2x}}{\omega \mu_2 d} \tau$$

then

$$\Gamma = \frac{k_{1x} - k_{2x}d^{-1}}{k_{1x} + k_{2x}d^{-1}}; \ \tau = \frac{k_{1x}}{k_{1x} + k_{2x}d^{-1}} \tag{2.38}$$

According to the second equation of Eq. 2.26, and using the same set of the parameters as well as setting $c^{-1} = d$, the following can be obtained:

$$
\begin{aligned}
k_{2x} &= \sqrt{k_1^2 bd - k_{1y}^2 c^{-1}d} \\
&= \sqrt{k_1^2 d^2 - k_{1y}^2 d^2} \\
&= k_{1x}d
\end{aligned}
\tag{2.39}
$$

All in all, a set of parameters are found to satisfy the reflectionless condition for all incident directions and frequencies as well as the polarizations:

$$\bar{\bar{\epsilon}}_2 = \epsilon_1 \bar{\bar{s}}; \ \bar{\bar{\mu}}_2 = \mu_1 \bar{\bar{s}}; \ \bar{\bar{s}} = \begin{pmatrix} s^{-1} & 0 & 0 \\ 0 & s & 0 \\ 0 & 0 & s \end{pmatrix} \tag{2.40}$$

To truncate the computation space, only a reflectionless surface is not enough, we must also require that the field in region 2 is absorbed during its traveling, which can be achieved by setting s as complex number. In general $s = \alpha + i\beta$. Then the fields in region 2 are:

$$\mathbf{E}, \ \mathbf{H} \propto e^{i(\alpha k_{1x}x + k_{1y}y)} e^{-\beta k_{1x}x} = e^{i(\alpha k_{1x}x + k_{1y}y)} e^{-\beta \omega \sqrt{\epsilon_1 \mu_1} x \cos(\theta)} \tag{2.41}$$

There is an exponential damping factor above, which is frequency dependent. The

dependence on frequency can be removed if we choose the imaginary part of s as $\beta = i\frac{\sigma}{\omega\epsilon_1}$, the damping factor is now $e^{-\beta\omega\sqrt{\epsilon_1\mu_1}x\cos(\theta)} = e^{-\eta\sigma x\cos(\theta)}$, where $\eta = \sqrt{\mu_1/\epsilon_1}$.

Although the boundary condition can absorb the light without reflection theoretically, the thickness of the boundary layer is still limited. No matter what conditions are set at the computation boundary, reflection can not be avoided there. One of the choices is to set a perfect mirror in the computation region boundary, the reflected light will be damped again traveling backward inside the absorbing boundary, then the effective reflection coefficient for the absorbing boundary is $e^{-2\eta d\cos(\theta)}$, where d is the depth of the ABS layer, factor 2 comes from the round trip. Although theoretically we can get negligible reflection by using very large σ, there is a large discontinuity at the surface between the free space and the ABS boundary layer, which will generate errors. In reality, σ is chosen to be a function of the position in the layer to smooth the changing refractive index. The effective reflection coefficient can be expressed as:

$$R(\theta) = e^{-2\eta\cos(\theta)\int_0^d \sigma(x)dx} \tag{2.42}$$

Usually a polynomial function is used for $\sigma(x)$ as: $\sigma(x) = (x/d)^m\sigma_{max}$, then the reflection $R(\theta) = e^{-2\eta\sigma_{max}d\cos(\theta)/(m+1)}$. The value for m is tested numerically, $3 \leq m \leq 4$ is found to be optimal for FDTD.

Above all, we only showed the UPML boundary condition for one surface $(x = 0)$. In a 3D FDTD model, we need six ABS surfaces to enclose the computational region. Similar formulas can be obtained for all other surfaces.

F.   Near to far field transformation

As we mentioned before, FDTD only simulate field values in a limited region. In many cases, one is interested in far field optical properties, such as the research in

scattering by small particles. From Maxwell's equation and using Green function derivations, two formulas are available for obtaining far field values from the near field values. The surface integral based on the surface equivalence theorem [11, 12].

$Surface\ integral\ method$:

$$\mathbf{E}_s(\mathbf{r}) = \frac{exp(ikr)}{ikr}\frac{k^2}{4\pi r}\mathbf{n} \times \int\int_s \{\mathbf{n}_s \times \mathbf{E}(\mathbf{r}') - \mathbf{n} \times [\mathbf{n}_s \times \mathbf{H}(\mathbf{r}')]\}$$
$$\times\ exp(-ik\mathbf{n}\cdot\mathbf{r}')d^2\mathbf{r}'$$

$Volume\ integral\ method$:

$$\mathbf{E}_s(\mathbf{r}) = \frac{k^2 exp(ikr)}{4\pi r}\int\int\int_v [\epsilon(\mathbf{r}'-1)]\{\mathbf{E}(\mathbf{r}') - \mathbf{n}[\mathbf{n}\cdot\mathbf{E}(\mathbf{r}')]\}$$
$$\times\ exp(-ik\mathbf{n}\cdot\mathbf{r}')d^3\mathbf{r}'$$

(2.43)

Although both near-to-far field mapping methods can give similar accurate results for materials with small refractive indices, we prefer the surface integral method. There are two reasons:

1. In simulating scattering by large refractive-index particles, the field values are very small inside the particle. The volume integral method will generate more error if using the same number of FDTD grids as the surface integral.

2. Surface integral mapping involves the 2D integral operation, which is faster than doing a 3D volume integral operation.

As an example, Fig. 8 shows the surface integral method results for the refractive index m=8.2252+i1.6808. For the volume integral method, to get similar accuracy, one has to use a much smaller grid size $\sim \lambda/120$ as shown in [13].
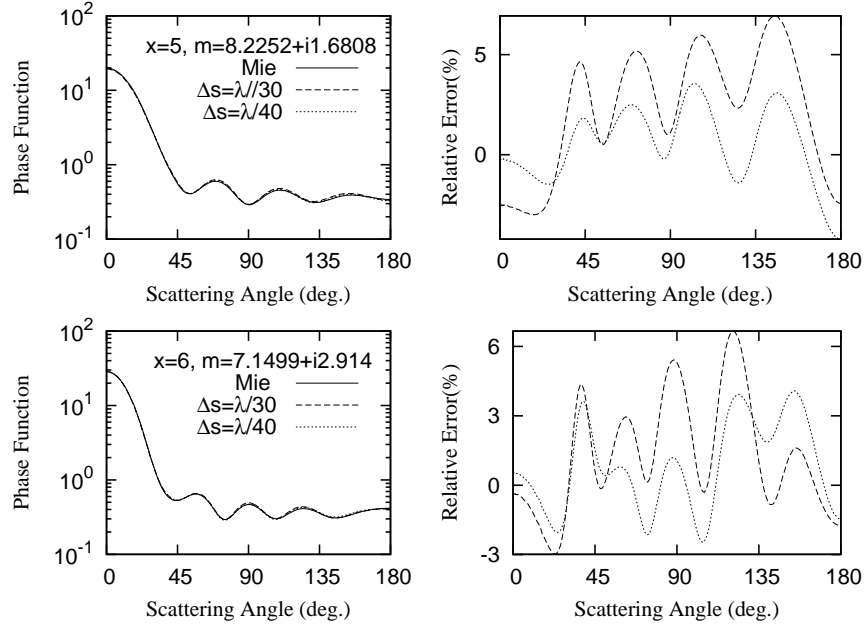
Fig. 8. Surface integral method for large refractive index case.

G.   Comparison with analytical results

To test the accuracy of our FDTD code, we simulate the sphere case and compare the simulation results with the Mie code as shown in Fig. 9.

We compare P_{11}, P_{12}, P_{33} and P_{34} elements with the Mie results, our results fit the analytical results very well except for several small regions in the side scattering direction.

H.   Conclusion

The FDTD method is a very powerful numerical method to solve Maxwell's equations in the time domain, it has many distinct advantages:

- It can simulate radiative interactions with models of complex morphologies and
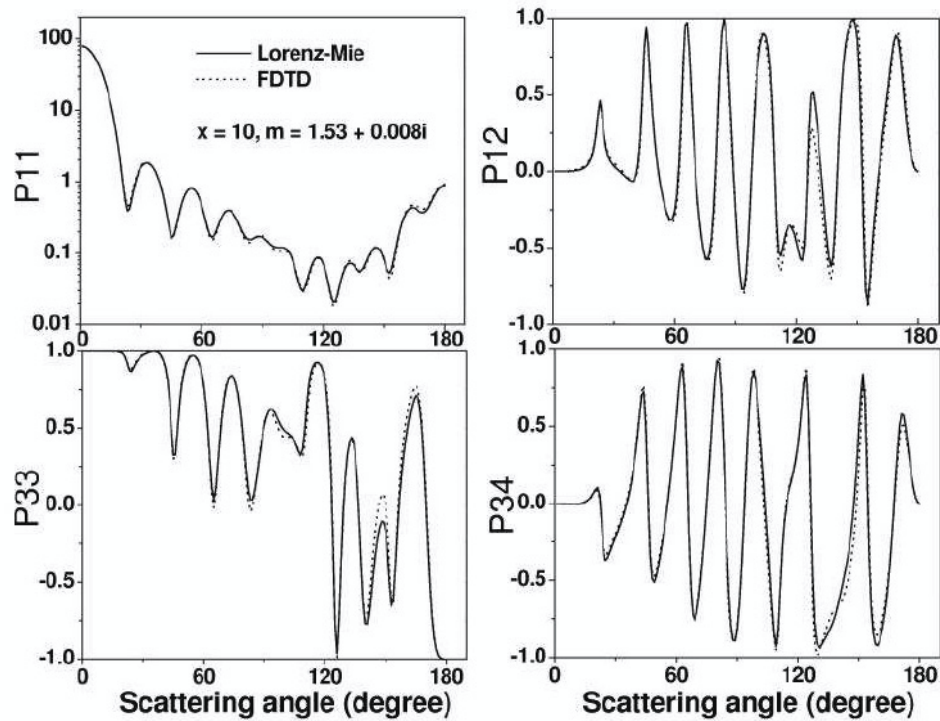
Fig. 9. Comparison with Mie results.

configurations;

- The simulation has high accuracy;

- It can simulate electric and magnetic fields in the time domain.

Although the FDTD method has gained great success, the required numerical computational time and memory consumption are usually quite a burden even with a supercomputer. Thus, improvements on the computational efficiency of the FDTD method are critical to its practical application.

CHAPTER III

PARALLEL FDTD

In the previous chapter, we have discussed the FDTD method. Although FDTD can simulate scattering from particles of arbitrary shapes and compositions with high accuracy, it has two obvious disadvantages: time- and memory-consumption, which greatly limits its applicability. Parallelizing the FDTD code can partially alleviate this problem. In this chapter, we described how to parallelize the FDTD using Message Passing Interface (MPI) technique [14] and compare the computation time with serial FDTD code. Although several researchers have already completed different versions of parallel FDTD code, there is no public source to obtain it up to now. During our parallelizing process, We have gained a great deal of help from Dr. R. Scott Brock (Department of Physics, East Carolina University) who completed another parallel FDTD code.

A.   Parallelization of the simulation region

In the previous chapter we have shown the basic idea of FDTD is to discretize the spatial and temporal region. Also, we note the spatial derivative in discretized FDTD grids are calculated locally, which means the operation needs only local field values. This character makes it possible to parallelize the simulation by separating the spatial region. Based on this idea, we have succeeded in parallelizing the serial FDTD code. Figure 10 shows an example for separating the computation region into two parts, each part is simulated by its own CPU and memory.

Unlike the parallelization method for Monte Carlo simulations, where every photon is independent of each other, the separated parts in the parallelized FDTD, such
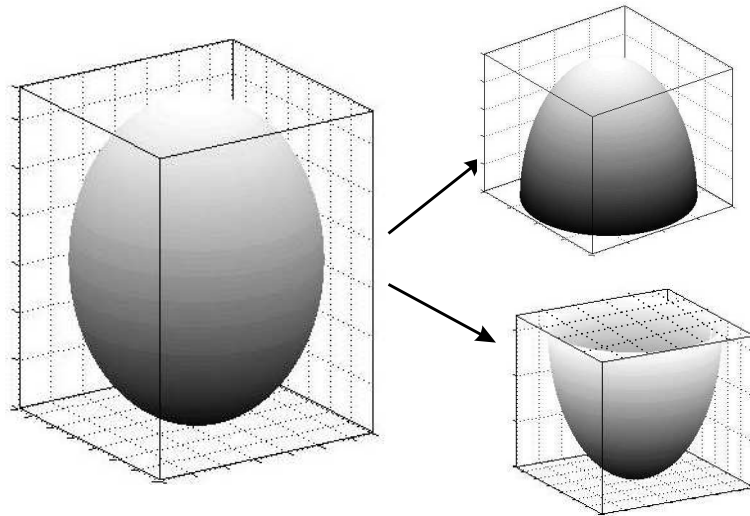
Fig. 10. An example to separate the computation region by two computing nodes.

as shown in Fig. 10, are not totally independent. The reason is that the fields on the surface of the cutting cross section need the fields of nearby nodes to update. We will demonstrate how to solve this problem after we introduce the parallel technique we used in the next section.

B. Introduction to MPI

We used Message Passing Interface (MPI) technique to realize the parallelization of our serial FDTD code. The reason for choosing MPI is simple: MPI is a standardized portable system. MPI, after it was created in 1990's, has become the standard parallel system for distributed memory parallel computer systems.

Figure 11 shows the structure of a distributed memory system. This system consists of many "computing nodes" from 1 to N and a fast network. Each node has its own CPU and local memory. The advantage of this system is obvious: it is scalable, which means within the capability of the network and the band width of data transfer, extra computing nodes can be added to the system without affecting

current nodes. In reality, thousands or even tens of thousands of computing nodes have been connected to build a super computer system. The essential role of the MPI is to control the messages sending and receiving from different nodes.
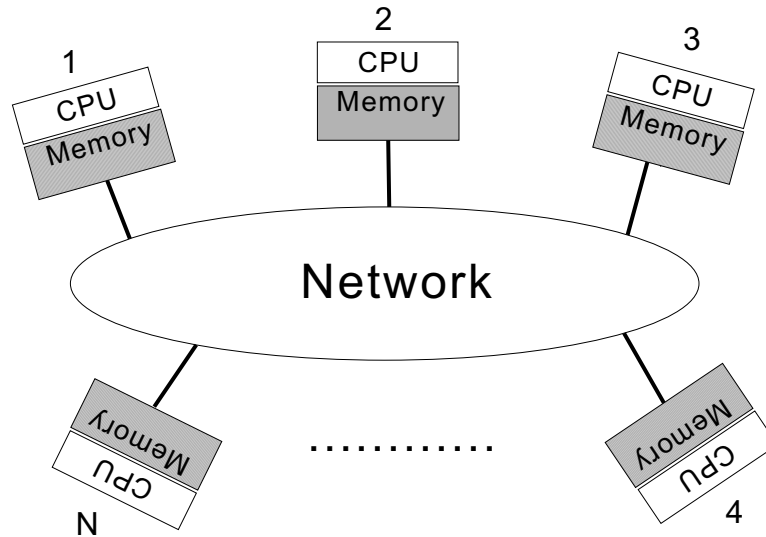
Fig. 11. Distributed memory parallel computer system.

In programming, MPI acts like an ordinary library, which contains lots of predefined variables and functions. Fortran, C and C++ can directly use those functions to implement the parallelization without worrying about how to control the network. For example, in our parallel code, MPI_SEND and MPI_RECV are frequently used. MPI_SEND can send values from the current computing node to the desired node we want, and the desired destination node uses MPI_RECV to accept values from the certain source node. We won't go into details of MPI in this dissertation.

C. Parallelization efficiency and conclusion

We have reviewed the basic ideas of MPI techniques. Now we will demonstrate how we use MPI techniques to deal with the cutting cross sections as described in the first

section of this chapter. Again we use a 2D FDTD example for clarity. In Fig. 12, the computation region was separated along the cutting line shown in the figure. We note that the left part , simulated in computing node n, contains the only magnetic field shown in the figure and the electric field are assigned to the right part, which is simulated by computing node n+1.
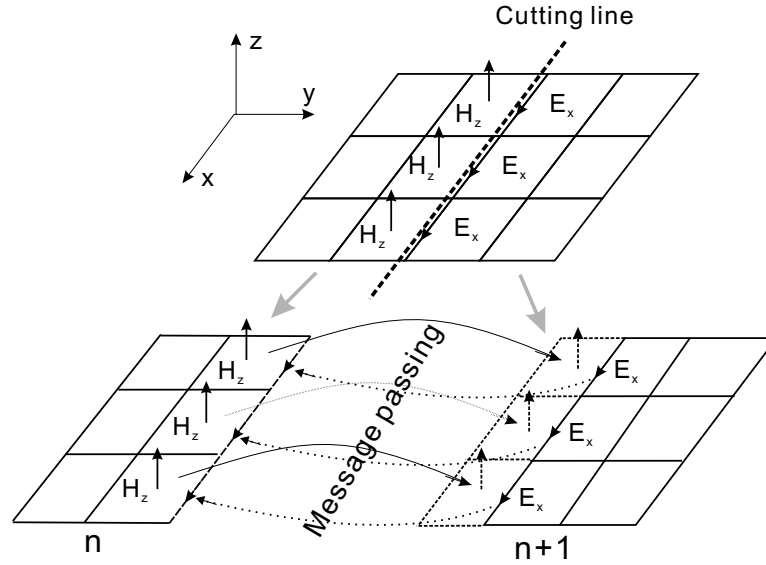
Fig. 12. Message passing between two nodes.

According to the FDTD formulas in the previous chapter, to update either the magnetic field or the electric field, we need them working together. That is to say that the computing node n needs values of electric fields in computing n+1, and computing node n+1 also needs the magnetic field values in computing n. As shown in Fig. 12, we need the technique called message passing to transfer the necessary field values between those two computing nodes. MPI is used to achieve this schema. For 3D FDTD model, the message passing is needed in a 2D cross section, more values are needed to be transferred between nearby computing nodes.

Figure 13 shows the flowchart of the complete parallelization of FDTD code. The

simulation process is as follows: it begins with the initialization of MPI parameters; then the computation region is divided and distributed to computing nodes; within each computing node, an independent FDTD simulation is carried out for electric fields; MPI functions transfer values of electric fields on the cross section to its previous nodes; magnetic fields are updated after receiving those electric field values from network; then MPI functions transfer magnetic field values on the cross section to its next computing node; after receiving magnetic field values, each computing node begins another loop of the whole process described above. The time loop will continue until preset time steps are reached. If far field values are required, the near-to-far field transformation will be carried out on each node after the time loop, finally MPI gathers simulation results from all the nodes to achieve a complete simulation.

Finally, we tested our parallel code efficiency by comparing that with serial code while simulating scattering by two different sizes of spheres. Our test is on the platform of an SGI Altix 3700 supercomputer of Texas A&M University. The result is shown in table I. The comparison clearly shows the great improvement for the computing time (Wall time), especially for large size parameters. Even with the fastest network, message passing from one node to another takes some time. If the particle is not large enough, the times consumed by MPI functions count more in total simulation time, which is likely the reason that parallelization works better for larger size particles.

Although parallel FDTD does not save computing time (summation of all cpu tims), it save wall time (the time one waited for the simulation). Taking advantage of the distributed memory structure, parallel FDTD can be used to simulate very large models, which the single pc can not. We also need to node that even in the most optimized condition, the wall time is inversely proportional to the number of

Initializing MPI Environment

Dividing Calculating Region

Initializing & calculating
FDTD parameters

Rank n   Rank n+1

Update E   Update E

MPI communication E

Time Loop   Update H   Update H   Time Loop

MPI communication H

Mapping   Mapping   Near-to-Far

Gathering values from all computing notes
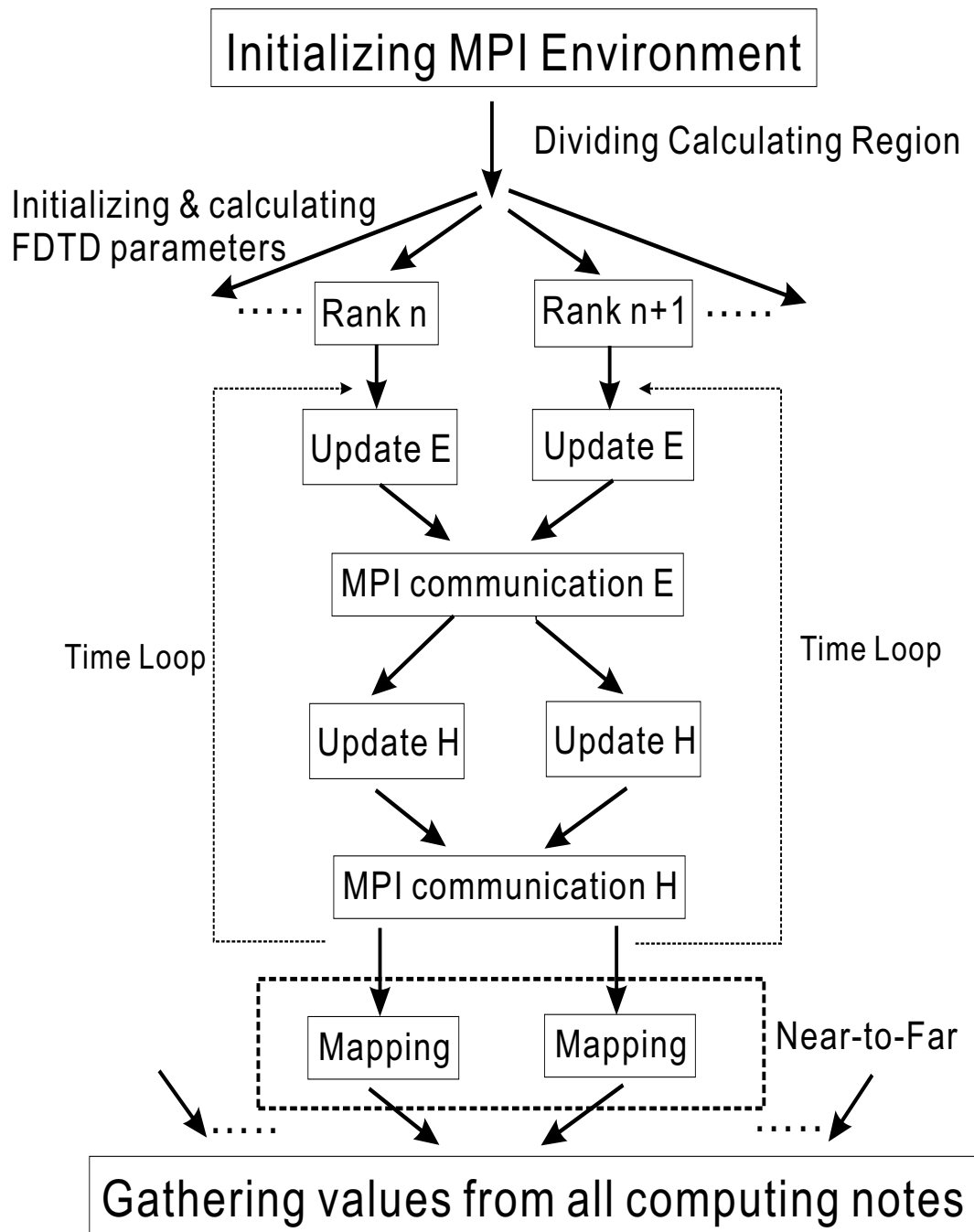
Fig. 13. The flow chart of our parallel method implemented in FDTD.

Table I. Comparison with serial code for different size spheres

size parameter	*single node* (*minute*)	*two nodes* (*minute*)	*four nodes* (*minute*)
x=10	27:18	20:53	13:07
x=15	166:45	75:56	41.09

computing nodes. At the same time, the computing time increase faster than cubic of the size scale. For large-scale models, only parallelization of the FDTD is not enough, we need to search other method to substantially decrease the FDTD grid number or computing operations, in which Pseudo-spectral Time-domain (PSTD) method [15, 16] is a good example which is already been applied to large-scale systems.

CHAPTER IV

THE EFFECTS OF PARTICLE SURFACE ROUGHNESS ON LIGHT

SCATTERING[*]

A. Introduction

The scattering of light by small particles is essential to atmospheric radiative transfer
[1], biological aerosol detection [17], remote-sensing technology [18] and other disci-
plines. The surface texture of a scattering particle, in addition to the overall particle
geometric shape, is an important morphological factor in determining the optical
properties of the scatterer. In the past two decades, the effect of asphericity of a par-
ticle on its single-scattering parameters (e.g., phase function and cross sections) has
been extensively investigated (e.g., Mishchenko et al. [19] and Wriedt [20] and refer-
ences cited therein). However, only a handful of studies have investigated the effect of
surface texture or roughness on particle optical properties. For particles with size pa-
rameters in the geometric regime, Macke et al. [21] and Yang and Liou [22] employed
the principles of geometric optics to study the optical properties of ice crystals with
surface roughness. It is quite challenging to compute the single-scattering parameters
of irregular particles with size parameters in the resonant region (i.e., where particle
size is of the same order as the incident wavelength) where the applicability of geo-
metric optics breaks down. In cases where the roughness scale is much smaller than
both the particle size and the wavelength, Schiffer used an approximation approach
[23, 24] to study particles from small size parameters to very large size parameters.

Also, many studies were done on deformed Gaussian spheres and spheroids using different methods such as the volume-integral equation approach by Lumme et al. [25], the second-order perturbation series by Nousiainen et al. [26], the FDTD method by Sun et al. [27]. Those kinds of roughness surfaces, on deformed Gaussian particles, have locally smooth surfaces without large slopes over most of the surface area. The roughness style in this chapter is very different. The surface becomes more locally "roughened" like the surface of a cell with microvilli. Several research works have been done on this kind of roughness [28, 29] using the discrete-dipole-approximation (DDA) method [30, 31]. Most recently, Sun et al. [32] used FDTD method to investigate the effect of surface roughness in two-dimensions for size parameters in the resonant regime. Since the scattering feature of a three-dimensional object is quite different from its idealized counterpart in a two-dimensional space, there is a need to investigate the roughness effect associated with a three-dimensional particle whose size parameter is in the resonant regime. It is noteworthy that surface roughness is often observed for natural particles such as ice crystals in cirrus clouds, biological spores in air or water, and animal tissue cells. Thus, the effect of particle surface roughness on optical properties is a subject that is of both theoretical and practical importance.

To simulate the optical properties of a roughened particle, one needs to define the surface roughness. Unlike methods used in [28] by randomly removing dipole elements on the surface, in this study we employed a well-controlled roughness model to determine the surface roughness, which specifies not only the total roughness area [29] but also the micro scale features of the roughness (width and depth) in a straightforward manner. Furthermore, we employ the finite difference time domain (FDTD) method to compute the phase matrix of roughened spheres. This chapter is organized as follows: In Section B the method used to specify particle surface roughness

is presented; in Section C the phase matrix of roughened spheres, computed from the FDTD method, is discussed in comparison with their counterparts for smooth spheres, and finally, the conclusions of this study are given in Section D.

B.   Pseudo roughness models

In this study, we investigated the effect of surface roughness for particles whose overall morphological shapes are spherical. In reality, the surface roughness of a natural particle is a morphological feature with random nature. To model a roughened surface, we use a simple mathematical scheme to define pseudo-random surface roughness. First we uniformly and randomly choose a number of points on the sphere surface. At each point, the region around this point is roughened: a "spike" given by the Gaussian distribution centered at the point is applied. Then the radial distances of the points in the vicinity of the selected point are of the form of

$$r(\theta, \phi) = R_0 \left[1 + \alpha A e^{\Delta\theta^2/2\sigma^2} \right] \tag{4.1}$$

where θ and ϕ are the zenith and azimuth angles of neighboring points; R_0 is the original radius of the sphere; A is a random number in the range$(-1.0 \leq A \leq 1.0)$, so the "spike" can be either outward or inward; $0 \leq \alpha \leq 1.0$ is a preset parameter; $\Delta\theta$ is the relative angle between the radial vectors pointing to center of the Gaussian spike and its reference point; and σ is the standard deviation of the Gaussian distribution used to control the size of the spike, which is important for the FDTD calculation.

To specify the surface roughness effect in light scattering computations, we define the degree of roughness by introducing a parameter:$\eta = 2\pi|m|\mu/\lambda$, in which $|m|$ is the absolute value of refractive index, λ is the wavelength, μ is the standard deviation of the radial distance obtained from standard statistical procedures: uniformly choosing

N (N≫1) sample points on the roughened sphere surface, we then calculate their radial distance (i=1,2,…,N) and their mean value $\bar{r}$, finally $\mu = \sqrt{\frac{1}{N-1} \sum_{i=1}^{N} (r_i - \bar{r})^2}$. In our pseudo-roughness sphere, $\bar{r}$ is approximately equal to original sphere radius . To ensure the validity of the FDTD method when it is applied to a particle with surface roughness, the scale of the roughness spike needs to be larger than the spatial grid used in the FDTD computation. In this chapter, we ensure that the scale of each roughness spike is at least three times larger than the grid size.

Figure 14 shows the morphologies of roughened spheres with various roughness conditions. Note that a perfectly smooth sphere is a special case of a roughened sphere when the roughness parameter $\eta=0$. The present method for specifying the roughness has several advantages in the sense that random numbers are used to determine the position and height of the roughness points. Thus, the final roughness surface has no symmetry. Additionally, the size of the roughness spikes can be controlled to ensure the FDTD method is reliable in simulation. Furthermore, the parameter η can be adjusted by changing the number of roughness points and their amplitudes.
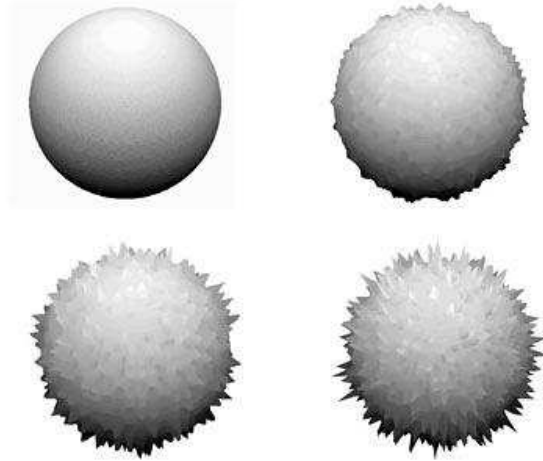

Fig. 14. Samples of surface roughness for spheres with increasing values of the roughness parameter η.

The parameter σ used to control the size of the angle in this chapter is very small (approximately between 1 and 2 degrees) to get the final surface structures shown in Fig. 14. To get similar roughness patterns using the Gaussian random sphere model, the correlation angle would have to be very small, and in that case, we couldn't guarantee the final roughness spikes were larger than the FDTD grid size, which is the reason we didn't use the Gaussian deformed sphere model in our calculations.

C. Phase matrix of particles with surface roughness

The roughened spheres studied in this chapter are homogenous with refractive index m=1.53+0.008i, typical of some aerosols. Different values of the parameter η are used for each size parameter. This parameter is not arbitrary because we must choose it in a reasonable range to keep the roughness relatively small compared with the original shape, which implies that large values of η can only occur for the large size parameter cases. To satisfy the requirement that the size of the spatial grid in the FDTD is less than the roughness spike as described in the previous section, we chose the grid size as $\Delta x = \lambda/40$ for x=5, $\Delta x = \lambda/30$ for x=10, 15 and 20 respectively.

For a smooth sphere, the phase matrix elements depend only on the zenith angle (angle between the scattered light and incident light); however, for roughened spheres, it will also depend on the azimuth angle. To compare our result with spheres, we choose a fixed scattering plane (fixed incident direction and azimuth angle) to compare the results and we averaged the roughened sphere results over random orientations.

Figure 15 compares the reduced phase matrix elements P_{11}, P_{12}, P_{33} and P_{34} for the case of size parameter x=5. To keep the overall morphological shapes close to spherical, μ is relatively small for these small particles. The first thing to note is that P_{11} agrees very well with the smooth sphere except at angles close to backscatter-

ing and there it reduces the glory value. The other reduced matrix elements show substantial differences for a large range of scattering angles.
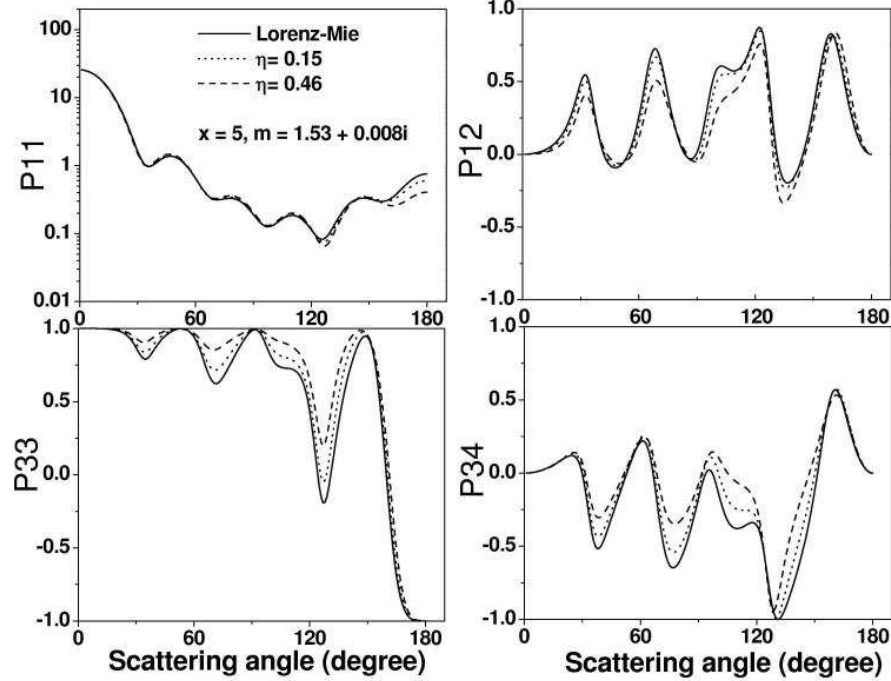
Fig. 15. Comparison between the reduced phase matrix elements computed from the roughened sphere and Lorenz-Mie calculations for a sphere with a size parameter x=5.

Figures 16, 17 and 18 compare the same elements shown in Fig. 15; however, they are for size parameters of x=10, 15 and 20 respectively. With the increase of size, a larger degree of roughness can be achieved without changing the overall morphological shape. Just as in Fig. 15, the results for small values (dotted lines in figures) keep the deviation of the phase function (P_{11}) from its spherical counterpart very small but the deviation gets larger with increasing size parameter. The other elements can deviate by very large amounts; however, what is noteworthy is the fact that the maxima and minima still keep their relative positions but the amplitudes

are in general reduced. The scattered light also becomes more unpolarized and this effect has also been noted in [32] using a 2D model. It is clear that when $\eta > 1$, the spherical approximation can't be used any more, otherwise substantial errors will be introduced.
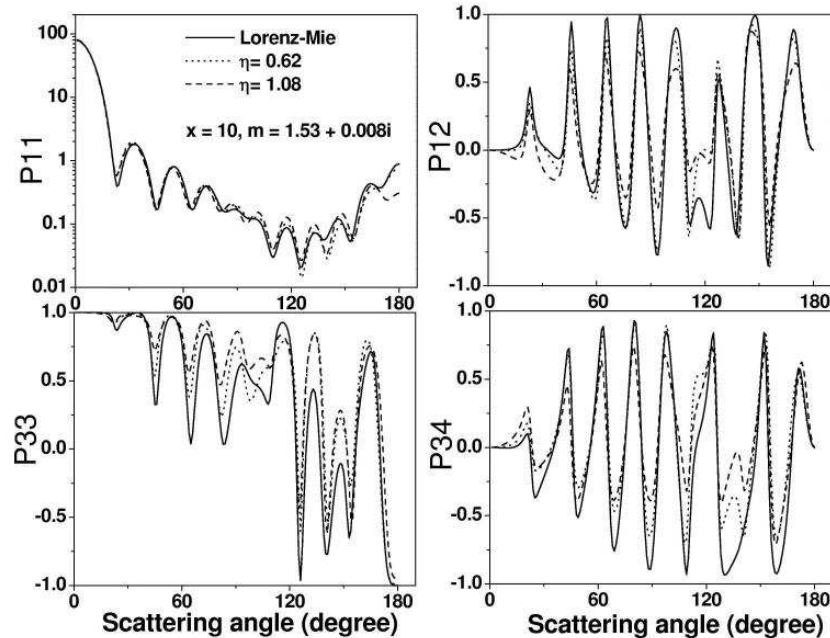
Fig. 16. Same as Fig.15 except for size parameter x=10.

Another interesting point to note is that the reduced matrix element $P_{44} = P_{33}$ for a sphere of any size, and this relationship held up remarkably well for the roughened spheres as well although the plot is not shown.

A good test of asphericity can be seen in the element P_{22}. We show this element in Fig. 19 for all the size parameters used in this chapter. The asphericity can be detected in this element for scattering angles in the backward direction
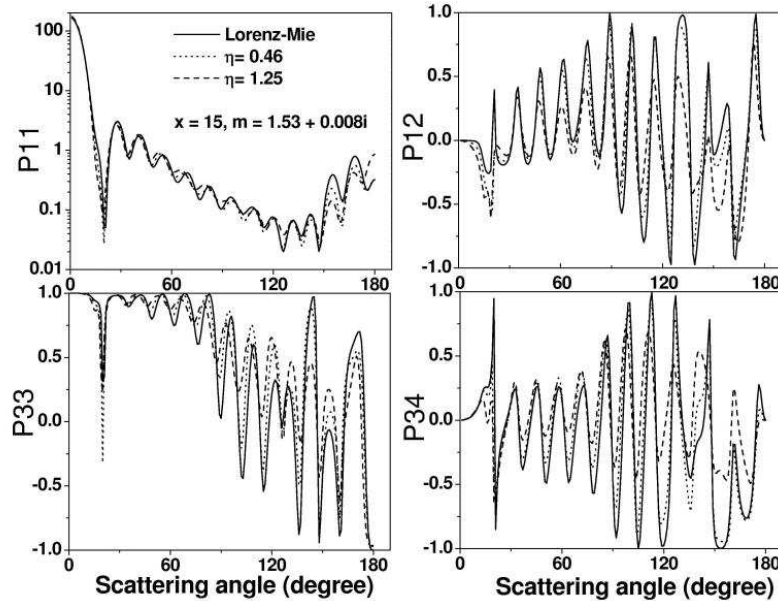
Fig. 17. Same as Fig.15 except for size parameter x=15.

D. Conclusions

In this chapter, we have studied the surface roughness effects for different size spheres. To specify the roughness, we introduced a degree of roughness parameter η , which is a measure of the relative size of the roughness compared with the wavelength. Our results show that for η <1 the effect of surface roughness on light scattering is relatively small as far as the phase function (P_{11}) is concerned; however, for the other phase matrix elements, substantial errors can be incurred at some scattering angles. For $\eta > 1$ and for the larger size particles, such as x>15, even the phase function can show substantial deviations from its spherical counterpart. The upshot of this analysis is that using spherical approximations for roughened particles can lead to large errors in the results especially when one is doing Mueller (phase) matrix imaging.
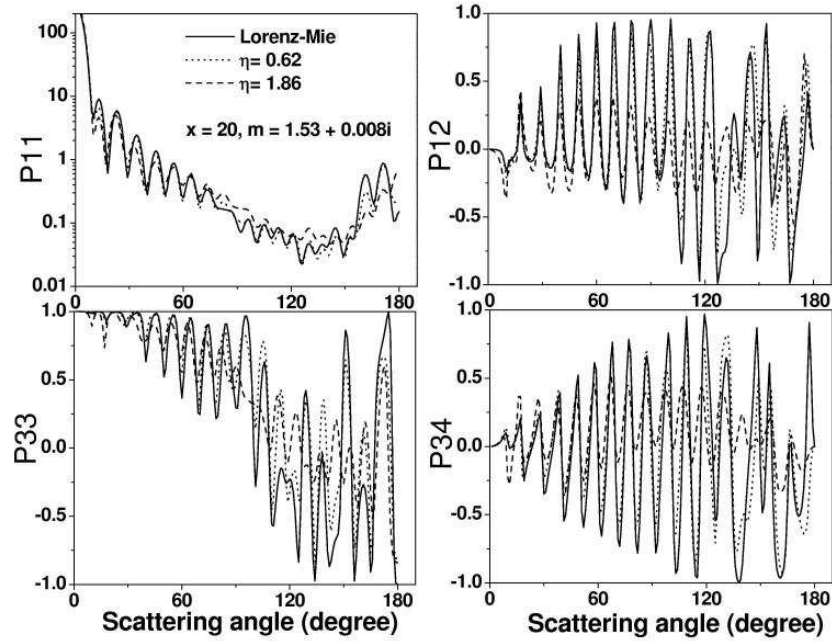
Fig. 18. Same as Fig.15 except for size parameter x=20.
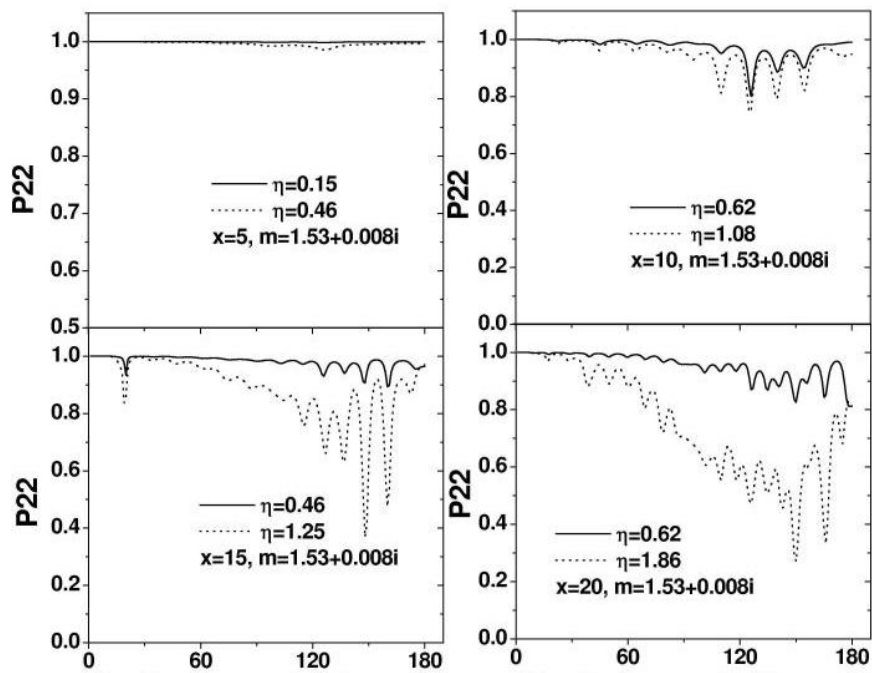
Fig. 19. Comparison of the reduced phase matrix element P_{22} (the element sensitive to asphericity) with a sphere which is always unity for all scattering angles.

CHAPTER V

BACKSCATTERED MUELLER IMAGES*

Bioaerosols such as spores, pollens, some viruses and cells have dimensions of the order of micrometers. There are large variations in both the morphology and composition of these particles. In recent years the detection and classification of bioaerosols, such as anthrax, has gained the attention of many research groups because of bioterrorism threats [33]. Of all the detection methods proposed thus far, DNA analysis is perhaps the most accurate. However DNA analysis not only requires complex equipment, it also takes a long time to complete. In reality, hazardous bioaerosols may be mixed with similar but benign particles, it then takes even longer in detection time for DNA analysis to separate the benign from the hazardous ones. Many methods have been applied and are under further research to speed up the analysis procedure, such as FASTCARs [34], fluorescence [35], etc. Images based on the Mueller matrix have previously been explored in studying optical properties of turbid media [36, 37], such as tissues. In this paper, we study light scattered from isolated single particles. With recent developments in detection schemes, complete backscattered light can be detected [17]. We have computed the backscattered Mueller matrix, and from it constructed angularly resolved Mueller images. There are three models used in this paper; namely, a homogenous ellipsoid, an ellipsoid with core, and homogenous cylinders. Since the sizes of these particles are comparable with the incident wavelength, geometric optics is not an option. We therefore used the finite-difference time-domain (FDTD) [1, 5, 6] technique to perform the numerical simulation involved in this study.

A.   Models and image construction

In our simulation, the models are constructed as shown in Fig. 20. They are: one homogenous ellipsoid (Fig. 20(a)), one spore (Fig. 20(b)) (same shape as the Fig. 20(a) but with inhomogeneous compositions) and homogenous cylinders with different heights (Fig. 20(c)). The refractive indexes for the homogenous ellipsoid and cylinder are m=1.34. In case of the spore model, the refractive index is chosen according to Fig. 20(d) based on the relative radial distance from the boundary. As described in [38], the spore model used in this chapter represents a spore with a core in the center and a single layer coat. In our simulation, the scatterers are placed in the air, which has refractive index m=1.0.
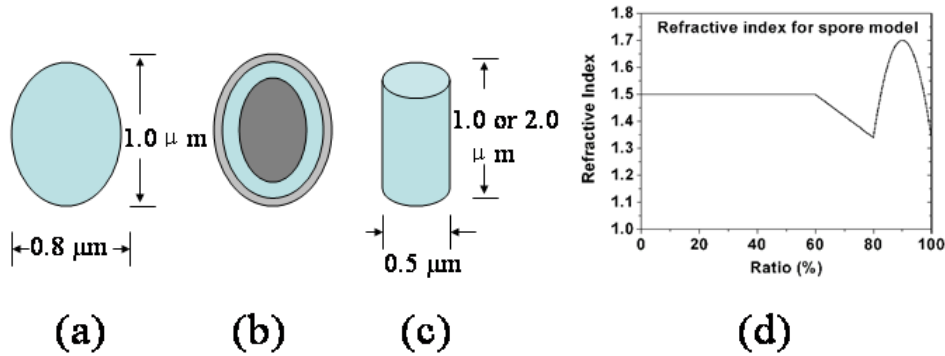
Fig. 20. Particle geometries used in this study: (a) a homogenous ellipsoid with a major axis of 1.0 μm and a minor axis of 0.8 μm; (b) the same ellipsoid with a centered core and one layer coat; (c) homogenous cylinders with heights 1.0 μm or 2.0 μm, and width 0.5 μm; (d) the refractive index for (b).

The backscattered region (polar angle from 90 to 180 degree) is the one we chose in this chapter. An actual experimental setup has been done in [17] as shown in Fig. 21, in which almost all the backscattered light can be detected.

The Mueller matrix is the transformation matrix between the incident Stokes
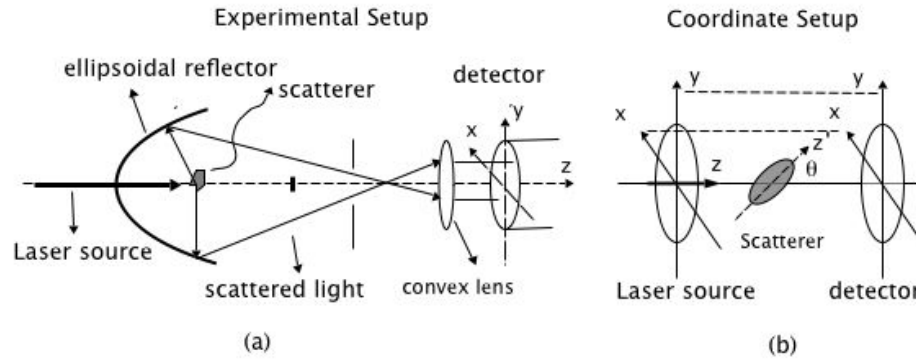
Fig. 21. (a) An experimental setup to measure the backscattered light in [17]. This experimental setup collects most of the backscattered light and projects it to the detector. (b) Coordinates used in this chapter. The scatterer is fixed in the yz-plane, θ is the angle between the symmetry axis of the scatterer and z axis.

vector and the outgoing Stokes vector. Since the Stokes vector is only meaningful when defined with respect to a coordinate system, Mueller matrix elements also depend on the coordinate system. Fig. 21(b) shows the coordinate system used in this chapter, the x, y, and z axes form a right-handed Cartesian coordinate system, where z is the direction of the incident illumination beam. To simplify the simulation process, the particle's symmetry axis is fixed in the yz plane. Mueller matrix elements are dependent on particle orientation (denoted by) and the scattering angle in the coordinate system defined here. For any given θ, the constructed images are angularly resolved images. The image has a disk shape with 180-degree polar angle at the center of total backscattering and the 90-degree polar angle at the boundary. The polar angle is uniformly divided along the radius in the image. The uniform division of the polar angle may not be satisfied in the experimental setup as shown in the Fig. 21(a).

B. Results of simulation

The Mueller matrix (M=$m_{i,j}(\theta, \phi)$, i,j=1,2,3,4) is a 4x4 matrix and therefore the corresponding complete Mueller images contain 16 sub-images. In this chapter, the reduced Mueller matrix is used, which means all values except $m_{1,1}$ are normalized by $m_{1,1}$. Thus all matrix elements except $m_{1,1}$ are in the region (-1,1). In Fig. 22, an example of the complete Mueller images is shown. These images show the simulation results of the homogenous ellipsoid as in Fig. 20(a) with an orientation angle of 90° (broadside illumination). The first image element $m_{1,1}$ represents the angular distribution of scattered light intensity with an unpolarized illuminating beam. The color bar of $m_{1,1}$ represents the values in the sense of the following equation:

$$\sigma = \frac{1}{k^2} \int m_{1,1}(\theta, \phi) d\Omega, \tag{5.1}$$

where the integral is over the whole 4 π steradian solid angle; is the scattering cross section, which equals to 2.23 μm^2 in this case for unpolarized incident light; k is the wave vector defined as $k = 2\pi/\lambda$ where λ is the wavelength. Since we are interested in the pattern character, values for $m_{1,1}$ in the following figures are not specified although the color scale in the image is from blue to red corresponding to the minimum and maximum values of $m_{1,1}$ in the backscattered region. The color used in all the other element images except $m_{1,1}$ scales from -1 to 1. It is worthy to note that values are zero along x and y-axis for elements ($m_{1,3}$, $m_{1,4}$, $m_{2,3}$, $m_{2,4}$, $m_{3,1}$, $m_{3,2}$, $m_{4,1}$, and $m_{4,2}$), which is because the particle simulated has mirror symmetry with respect to the xz and yz-plane.

As mentioned earlier, Mueller images depend on the orientation of the scatterer, each orientation has a unique 4x4 Mueller image. In Fig. 23, three orientations with polar angle $=0^o, 30^o$ and 90° are simulated. To compare the differences in Mueller
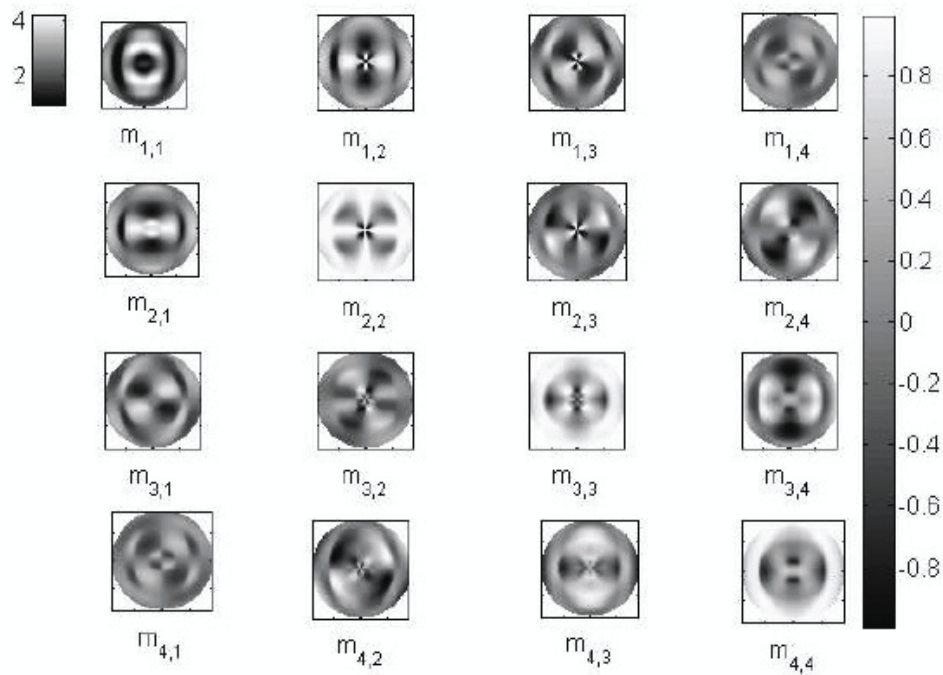
Fig. 22. A complete set of Mueller images for broadside illumination of the homogenous ellipsoid with a major axis of 1.0 μm and a minor axis of 0.8 μm, the refractive index is 1.43 and the illuminating wavelength is 0.5 μm.

images of different shapes and compositions, $m_{1,1}$ and $m_{4,4}$ are used as representatives for Mueller images.

Figure 23 shows the comparison between the homogenous ellipsoid and the spore model. For Mueller images of $m_{1,1}$ and $m_{4,4}$ there are significant differences. The presence of the core and the coat greatly changes the backscattered image pattern. The spore gives more fine structure in the $m_{4,4}$ images. One can also see the scattering patterns change with the orientation angle. From these patterns, it should be possible to retrieve the composition and orientation information.

Figure 24 compares the scattering image patterns for the homogenous ellipsoid, the spore with core and coat and a homogenous cylinder with height 1.0 micrometer.
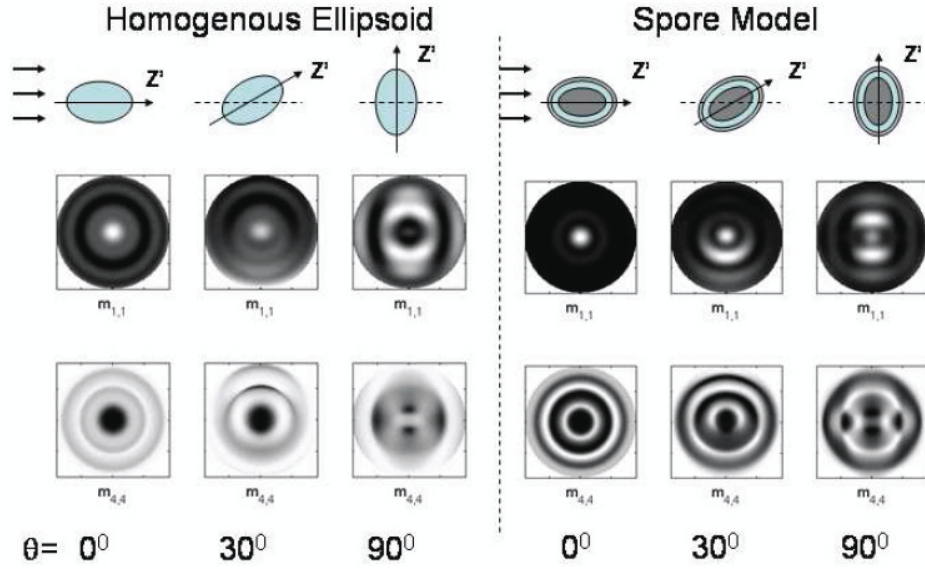
Fig. 23. Comparison for Mueller elements $m_{1,1}$ and $m_{4,4}$ between homogenous ellipsoid and spore with a core at different orientations. Both particles have a major axis of 1.0 μm and a minor axis of 0.8 μm, the illuminating wavelength 0.5 μm.

They are all broadside illuminated, i.e.,$\theta = 90^o$. Although the three small particles are similar in size scale compared with the wavelength of the illuminating beam, there are distinct differences in the patterns between the cylinder's images and the ellipsoid's. One can easily distinguish the cylinder shape from the ellipsoid shape.

To study how the size affects the scattering patterns, we doubled the height of the cylinder while keeping the radius unchanged. The results are shown in Fig. 25. Overall the patterns for these two cylinders are similar. The increase in the height brings more fine structure. Size information could possibility be derived from these fine structures.

To compare with forward scattering results, in Fig. 26 we calculated forward scattered Mueller images for the same case as used in Fig. 24. There is less infor-
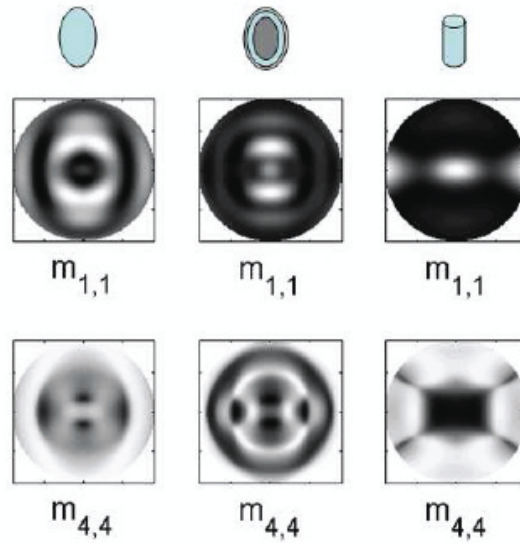
Fig. 24. Comparison for Mueller element $m_{1,1}$ and $m_{4,4}$ between homogenous ellipsoid, spore and homogenous cylinder for broadside illumination.
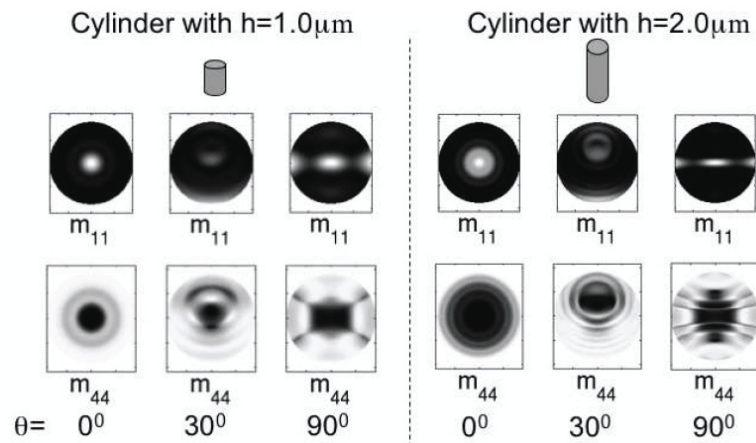
Fig. 25. Comparison for Mueller element $m_{1,1}$ and $m_{4,4}$ between homogenous cylinders with different height 1.0 μm and 2.0 μm, and same diameter at 0.5 μm, refractive index at 1.34 and illuminating wavelength at 0.5 μm.

mation contained in the forward scattering pattern compared with results in Fig. 24. For three $m_{1,1}$ images, their patterns look similar, which means that forward scattering $m_{1,1}$ is not as sensitive to the shape and internal structures as for the $m_{4,4}$ images. Although there are some differences in regions away from the center for $m_{4,4}$, the differences are not as distinct as backscattered images. This is the reason we feel backscattering is more important in classifying aerosols.
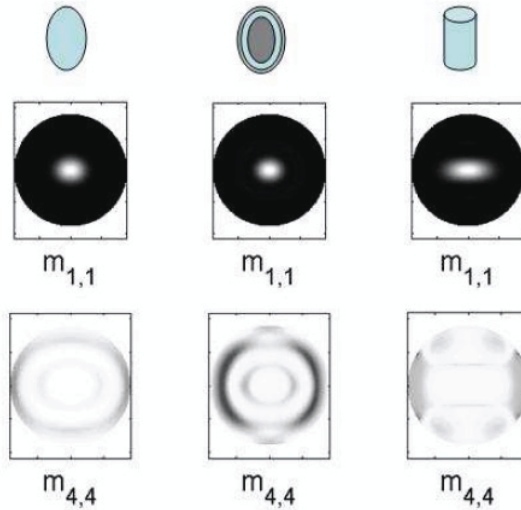
Fig. 26. Same as Fig. 24 except for the Mueller images for forward scattering.

C. Discussion and conclusions

In this chapter, backscattered Mueller images are simulated for several small dielectric particles whose sizes are comparable to the wavelength of the illuminating light. Compared with forward scattering results as shown in Fig. 26, backscattered Mueller images are much more sensitive to the shape, size and composition of the particle. Even in the simplest case where only the scattered intensity is detected with an unporlarized illuminating source, backscattered intensity image ($m_{1,1}$) still shows more

variation between different cases. However, when the polarization is taken into account, the other Mueller images contain more pattern variations. To obtain complete identification would require solving the inverse problem, which will be quite difficult to do. However even without inverse methods, one can setup databases for known particles and do pattern recognition to distinguish different kinds of particles. In addition to the classification of particles, the results shown in this chapter can be applied to rapid detection of hazardous biological agents. Together with proper experimental setup (such as the one shown in [17]), pattern recognition can be used to identify particles having similar Mueller images as the hazardous biological agents stored in the database. The selected particles can then undergo further analysis by other methods, such as DNA analysis. The sample number is greatly minimized as well as the total detection time. Since this method uses the strong elastic scattered signals, it does not require sophisticated equipment for signal amplification. The simulations in this chapter are only for a single particle. It is straightforward to apply this simulation to clusters. We also want to explore the possibility of using two wavelengths and looking at differences in the Mueller images.

CHAPTER VI

RADIATIVE ENERGY FOR DIELECTRIC PARTICLE ILLUMINATED BY A
PLANE ELECTROMAGNETIC WAVE*

We have studied the distribution of the electric and magnetic energy densities within and in the vicinity outside a dielectric particle illuminated by a plane electromagnetic wave. Numerical simulations were performed by using the Lorenz-Mie theory and the finite-difference time-domain method for spheres and spheroids, respectively. We found that the electric and magnetic energy densities are locally different within the scatterers. The knowledge of the two components of the electromagnetic energy density is essential to the study of the dipole (electric or magnetic) transitions that have potential applications to Raman and fluorescence spectroscopy.

A. Introduction

For a plane electromagnetic wave propagating in a homogenous medium, the energy densities of the electric and magnetic components are uniform and locally the same; however, in the presence of a scatterer, the energy density within the scatterer is not uniform. In this study we investigate the relationship between electric and magnetic energy densities within and in the vicinity outside small scatterers. A great deal of research has been done on the internal electric field within infinite cylinders and spheroids [39, 40, 41], as well as in irregularly shaped particles [42]. However, these previous studies concentrated on the electric field or intensity within and in the vicinity outside the particles. To our knowledge no one has shown the corresponding

---

magnetic field distribution in the same region, which may be important in many practical applications. In this study, we computed the energy densities associated with both the electric and magnetic fields for two particle geometries; namely a sphere and an ellipsoid, with two different refractive indices. The sizes of these particles are comparable with the incident wavelength, which rules out geometric optics. We therefore use the Lorenz-Mie theory for the sphere and the finite-difference time-domain (FDTD) [5, 6, 43, 44] technique for the ellipsoid to perform the numerical simulation involved in this study. However various other methods have been developed for computing the scattering properties of nonspherical particles and these were recently reviewed by Mishchenko et al. [45]. The three-dimensional FDTD computational program that we used was developed by Yang et al. [43] and has been enhanced by using the Uniaxial Perfectly Matched Layer (UPML) boundary condition [10]. The validation of the improved FDTD computational program has been reported by Li et al. [46] by comparing with the exact solution for the scattering of light by spheres. This chapter proceeds as follows: presented in Sec. B are the particle morphologies and the definitions of the electric and magnetic energy densities; the results of the simulations are shown in Sec. C; and finally, the potential applications of this study are discussed in Sec. D.

B.   Models and definitions

We consider two particle shapes; namely a sphere and an ellipsoid as shown in Fig. 27. The diameter of the sphere is 1.0 μm. The aspect ratio of the ellipsoid is 1.96, and has the same volume as the sphere.

The illuminating light source in the present simulation is an unpolarized plane wave, and therefore polarization effects are not considered. Since the electric and
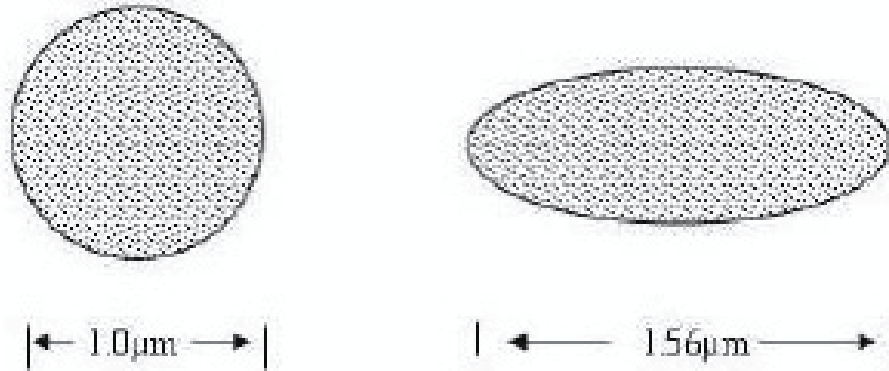
Fig. 27. Particle geometries used in this study: a homogenous sphere with a diameter
of 1.0 μm and a homogenous ellipsoid with a major axis of 1.56 μm and a
minor axis of 0.8 μm. The two particles have the same volume.

magnetic fields are time-dependent, we consider the temporally averaged values of
the fields. The electric and magnetic energy densities of an electromagnetic wave are
defined as follows [47]:

$$u_e(\mathbf{r}) = \frac{1}{2}\epsilon(\mathbf{r}) < E^2(\mathbf{r}) >,$$
$$u_h(\mathbf{r}) = \frac{1}{2}\mu(\mathbf{r}) < H^2(\mathbf{r}) >,$$

(6.1)

where ϵ and μ are the permittivity and permeability of the medium respectively.
$< E^2 >$ and $< H^2 >$ indicate the temporally averaged field values. The densities
defined in Eq. 6.1 are proportional to the incident irradiance that is set to unity in
this study.

C.   Results of simulation

Figure 28 shows the distributions of both the electric and magnetic energy densities
inside and in the vicinity outside the sphere described in Fig. 27, which were computed
on a vertical cross section through the center of the particle and parallel to the incident
radiation. The incident wavelength and the refractive index of the sphere are λ=0.3

µm and m=1.34, respectively. Due to the large range in values (as in Fig. 29), a logarithmic scale is used. Evidently, the intensities inside the particle are not uniformly distributed. Both of the electric and magnetic fields are focused in the forward direction along the incident light. The overall patterns of the energy density distributions for the two field components are similar, and the differences between the electric and magnetic energy densities are essentially quite small except in a focal region shown in the panel (c) in Fig. 28.
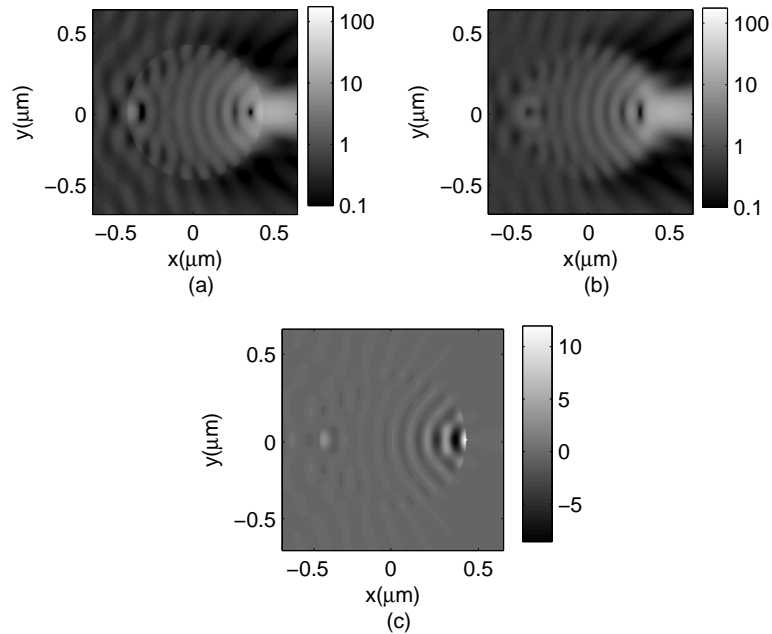
Fig. 28. Internal and near-field electric and magnetic energy densities and their differences. The incident wavelength and refractive index for the simulation are λ =0.3 µm and m = 1.34, respectively. (a) The electric energy density; (b) the magnetic energy density; and (c) the differences between the two densities (the electric energy density minus the magnetic energy density). One should note the jet like behavior outside the particle in the forward direction.

Figure 29 shows a case for a refractive index of m=2.0. As in the previous case, both the energy densities are focused in the forward direction near the edge of the

scatterer, where significant maxima are noticed for both the electric and magnetic energy densities. Additionally, the high energy density region moves toward the back of the sphere. The differences between the two energy densities are quite large in the focal region.
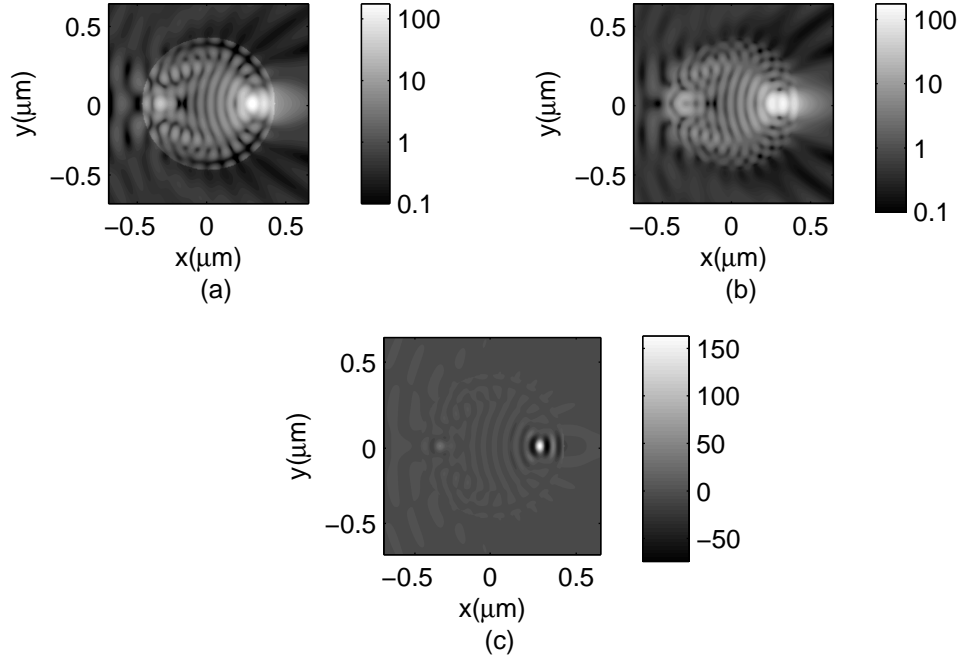
Fig. 29. Same as Fig. 28 except for refractive index of m=2.0. Also we note similar jet like pattern as in Fig. 28.

Figure 30 shows the distributions of the two energy densities and their differences for an ellipsoid. The ellipsoid has a major axis of 1.56 μm and a minor axis of 0.8 μm, and has the same volume as the sphere defined for Figs. 28 and 29. The incident wavelength and the refractive index of the scattering particle are chosen as λ =0.3 μm and m=1.34, respectively, which is same as the case in Fig. 28. The incident light is parallel to the major axis of the ellipsoid (as shown in Fig. 30). Similar to the cases in Figs. 28, the fields are also focused in the forward direction, but the energy density maxima located inside the particle are stronger in the case for the ellipsoid.

The differences of the two energy densities are not substantial except in the focal region, as is evident from the panel (c) in Fig. 30.
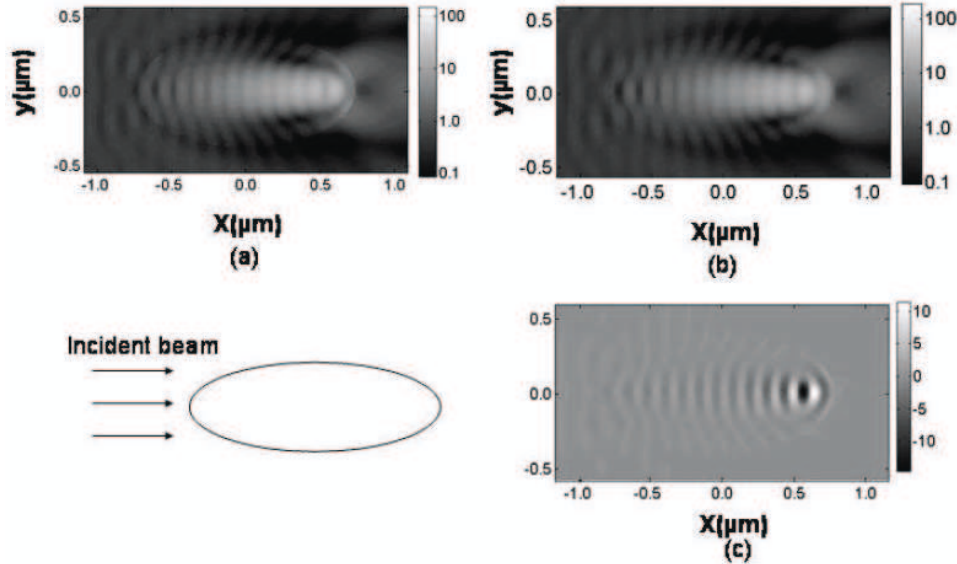
Fig. 30. Same as Fig. 28, except that the shape is an ellipsoid.

Shown in Fig. 31 are the results similar to those in Fig. 30, except that the ellipsoid is illuminated with broadside incidence. The energy density distributions are similar to a case where the incident light passes through a convex lens; however, there is not an explicit focal point in the present results. Inside the ellipsoid, the energy density differences are noticed primarily near the front boundary and in the nearby region. Outside the particle, the energy density differences are insignificant.

D. Discussion and conclusions

We also calculated two more spherical cases, one with diameter increased to 2 μm, refractive index m=1.34, the other one with diameter 1 μm as well as an absorptive refractive index m=1.34+i0.05. The field patterns are similar with Fig. 28, only
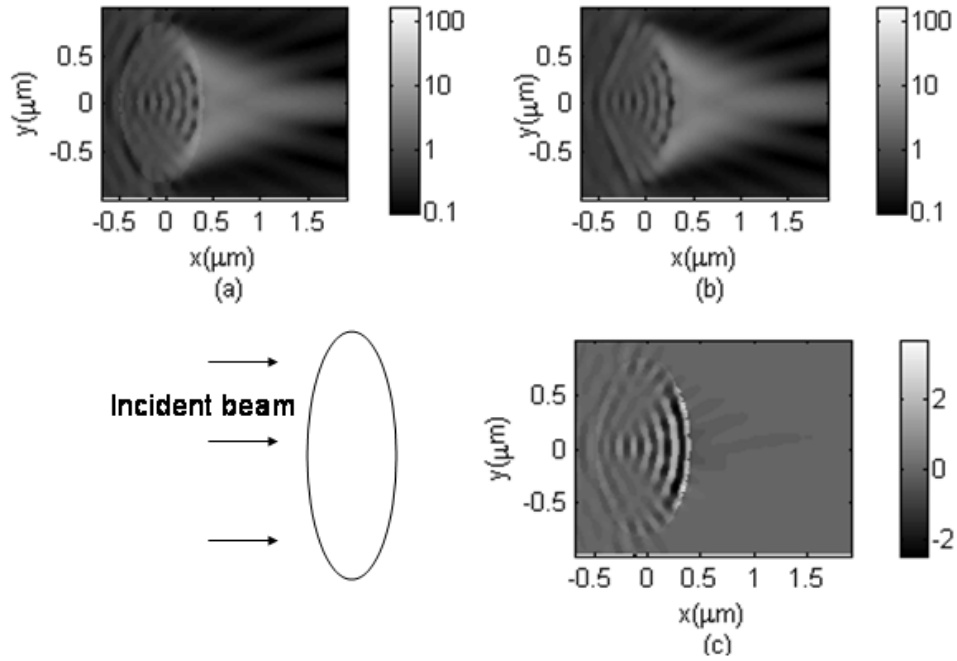
Fig. 31. Same as Fig. 30, except that the incident beam is perpendicular to the axis of symmetry.

major differences are that for those larger size sphere.

The distributions of both the electric and magnetic energy densities are essential to the study of light-induced reactions. In most cases, only the electric field is considered because the electric dipole transitions are more important in studying the interactions of radiation with matter. Note that the electric dipole transitions are normally $10^4 \sim 10^5$ stronger than the magnetic dipole transitions. However, in some cases the electric dipole transition is forbidden, such as for the case involving the 1s to 2s transition in an atom, in which the magnetic dipole transition plays an important role and then the magnetic field distribution must be considered. As shown by the present results, the distributions of electric and magnetic energy densities are not the same inside a scattering particle, and the local differences of these two energy densities can be quite large in a certain region within the scattering particle, partic-

ularly for cases involving large refractive indices. Since biological spores may have large refractive index component parts (core, shell, etc), the larger difference between the electric and magnetic fields inside the spore should be considered when they are being detected by using Laser induced Raman or fluorescence techniques. The highly concentrated radiation (shown in Fig. 29) inside the scatterer may alter the physical structure locally because the field intensity is magnified hundreds of times. The jet like behavior of the near-field intensity shown in Figs. 28 and 29 has also been described in [48], and may be applied to near-field scanning techniques [49]. It may also be useful for studying fluorescence and Raman effects.

CHAPTER VII

ELECTRIC DIPOLE RADIATION

In previous chapters, we have studied several aspects of elastic scattering by small dielectric particles with an external illuminating source. As we mentioned in Chapter I, radiative interactions with materials not only include elastic scattering, they also include inelastic scattering where different frequency electromagnetic waves are emitted, such as in Raman scattering. Raman scattering is due to both vibration and rotation of certain molecules. Besides radiative induced reactions, physical and chemical processes can induce certain molecules to emit electromagnetic fields, such as some kinds of fluorescence. Both Raman scattering and fluorescence are very important in remote sensing, biological agent detection and cell structure identification. In many cases, molecules that emit new frequency electromagnetic waves are embedded in small size particles which are comparable to the wavelength, such as biological spores, aerosols and cells. Compared with the particle size and wavelength, the molecule that emits electromagnetic waves can be treated as a point light source. Although the emission from molecules is a quantum process, from a classical point view, an electric dipole is usually used to model the emission process. Then it is very important to simulate the radiation from infinitesimal electric dipoles embedded in small particles with arbitrary shapes and compositions. Analytical calculations are available for homogenous spheroids and cylindrical particles [50, 51, 52]. Based on FDTD techniques [5, 46], we have developed an innovative numerical method to simulate infinitesimal electric dipole radiation within arbitrary shaped particles. Our results are consistent with the analytical results for sphere cases. The simulation results show the radiated field not only depends on the dipole itself, but it also depends on the position of the dipole, the shape and refractive index of the particle.

A. Dipole radiation in FDTD formulation

In our simulation method, as shown in Eq. 7.1, the dipole source is a Gaussian
function in the time domain. The simulation also assumes the dipole is a "hard"
source, that is the strength of the dipole is independent of the local electric field.

$$\mathbf{p}(t) = \mathbf{p}_0 e^{-(t-T_0)^2/\sigma^2} \tag{7.1}$$

where $\mathbf{p}$ is electric dipole defined as: $\mathbf{p} = \int_v \rho(\mathbf{r})\mathbf{r}d\mathbf{r}$; σ and T_0 are parameters con-
trolling pulse shape and the time delay. The vector potential generated by the in-
finitesimal dipole is:

$$\mathbf{A}(\mathbf{r}, t) = \frac{\mu}{4\pi r}\dot{\mathbf{p}}(t - \frac{r}{c}) \tag{7.2}$$

where the speed of the light c is the speed in the medium. From the vector potential,
the magnetic field can be calculated:

$$\mathbf{B} = \nabla \times \mathbf{A} \tag{7.3}$$

According to Maxwell's equations Eq. 2.1, the electric field can be calculated
from the temporal integral of the curl of magnetic field.

$$\begin{aligned} \mathbf{E}(\mathbf{r}, t) &= \frac{1}{\epsilon}\int_0^t \nabla \times \mathbf{H}(\mathbf{r}, t')dt' \\ &= \frac{1}{4\pi\epsilon}\nabla \times \left[\nabla \times \frac{\mathbf{p}(t - \frac{r}{c})}{r}\right] \end{aligned} \tag{7.4}$$

where $\mathbf{H} = \mathbf{B}/\mu$ as defined in Chapter II. The results of the above equations are very
complicated, and we show them in Appendix C.

When compared with the FDTD grid size, the dipole itself is assumed to be a
point source. In our method, as shown in Fig .32, the dipole is embedded inside a
FDTD grid. The electric field radiated from the dipole is calculated along the FDTD
grid edges. These fields act as the source term similar to the external source described

in Chapter II.
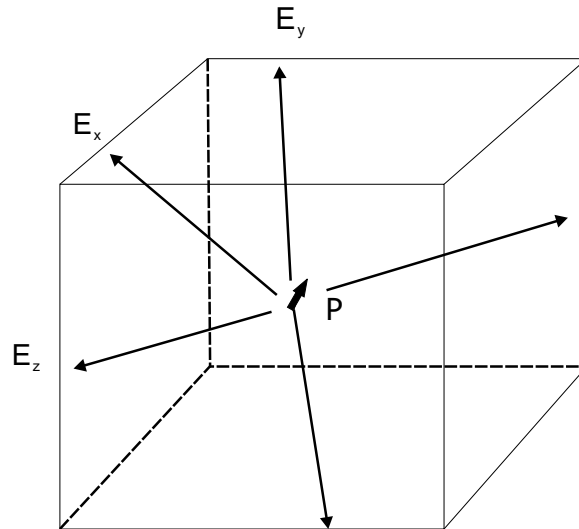
Fig. 32. The infinitesimal electric dipole model in FDTD grid.

The electric field values along the edges as shown in Fig. 32 are sensitive to the relative position to the dipole as well as the direction of the dipole itself. In general the direction of the dipole can be arbitrary, the electric field values at the center of the edges may not represent the average values along the edges. Modifications of the FDTD described in Chapter II, where the changes in fields are assumed to be locally approximately linear within grid cells, are needed. The modification is on the temporal updating of magnetic field on the nearby cube surfaces. One example is shown in Fig. 33. On the shaded area, Faraday's law (doing surface integral on both sides of Eq. 2.1 in Maxwell's equations) tells us that:

$$\int_l \mathbf{E} \cdot d\mathbf{l} = \frac{\partial}{\partial_t} \int_s \mathbf{H}_z ds',$$
(7.5)

where the path integral is along the direction shown in the figure. As described in Chapter II, except for the edge which is nearest to the dipole, the path integral

of the electric field along the edge is approximately equal to the value at the edge center multiplied by the grid size. The surface integral for the magnetic field is also approximately equal to the area times the field value at center of the area. Only the nearest edge to the dipole needs the path integral operation. After several simple mathematical derivations, in the descritized space and time, the temporal updating of $H_z(I, J, K + 1/2)$ is now obtained.

$$
\begin{aligned}
H_z^{n+1/2} & \left(I, J, K + \frac{1}{2} \right) \\
= & H_z^{n-1/2} \left(I, J, K + \frac{1}{2} \right) \\
& + \left\{ \frac{c\Delta t}{\Delta x} \left[E_y^n \left(I - \frac{1}{2}, J, K + \frac{1}{2} \right) - E_y^n \left(I + \frac{1}{2}, J, K + \frac{1}{2} \right) \right] \right. \\
& \left. + \frac{c\Delta t}{\Delta y} \left[\int_I^{I+1} E_x^n \left(l, J + \frac{1}{2}, K + \frac{1}{2} \right) dl - E_x^n \left(I, J - \frac{1}{2}, K + \frac{1}{2} \right) \right] \right\} \quad (7.6)
\end{aligned}
$$
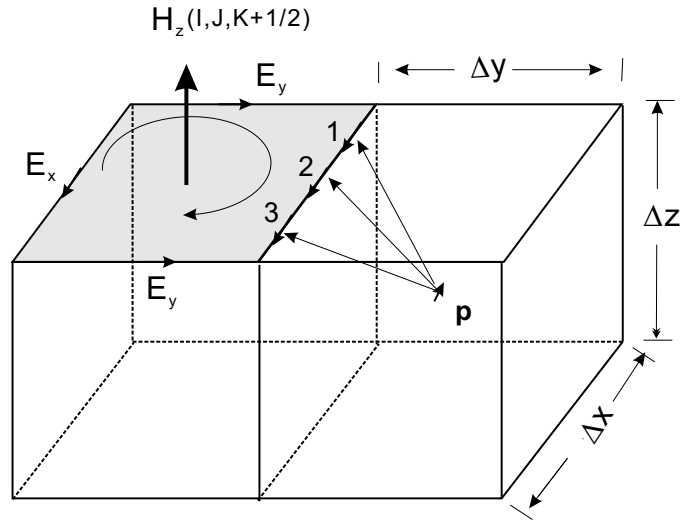
Fig. 33. Modification of FDTD in simulating dipole radiation.

B. Simulation results

To get the frequency domain results, as described in Chapter II, Fourier transformations will be carried on the temporal fields values of both the dipole source and the FDTD simulated fields.

Since analytical results for dipole radiation are available for a dipole embedded in a dielectric sphere, we first compare our FDTD results with analytical results to validate the accuracy of our simulation method.

In Fig. 34, we compare our FDTD results with analytical results [51]. The model we use are homogenous spheres with refractive index m=1.33, and the environment outside each sphere is vacuum. The normalized radiation is the ratio of the radiation from current model and the radiation of the dipole in infinite vacuum space. Fig. 34(a) shows the comparison for the total radiation vs. the size parameter, where the dipole is in the center of the sphere. Fig. 34(b) shows the total radiation from a sphere with fixed size parameter $x = 4$, while the dipole position changes from the center to the boundary of the sphere, and the direction of the dipole is perpendicular to the radial direction as shown in the figure. Our FDTD results fit the analytical results very well except for the small size parameter.

The next comparison with the analytical result is to compare the angular distribution of the radiated field in the far field. As shown in Fig .35, the sphere has size parameter of 8 and the refractive index is 1.33. The dipole is located at the 1/4 of the diameter of the sphere with the radial direction. The results are normalized to their maximum values. Again, the FDTD results fit the analytical results very well.

We also compare the results with the Discrete-dipole approximation (DDA) method [30, 31] results for other non-spherical shape models. In Fig. 36, the far
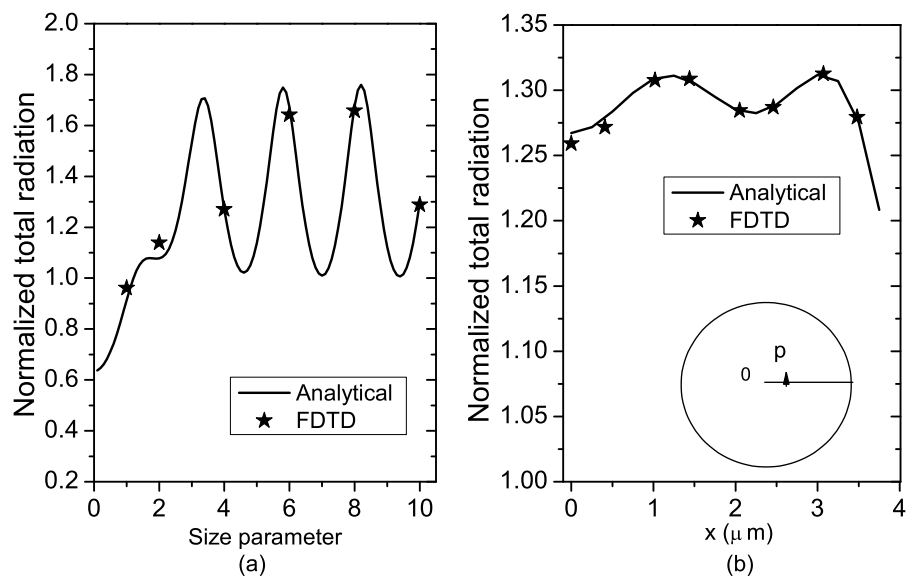
Fig. 34. Comparison of total radiation: (a) Total radiation vs. size parameter; (b) Total radiation vs. position of the dipole.
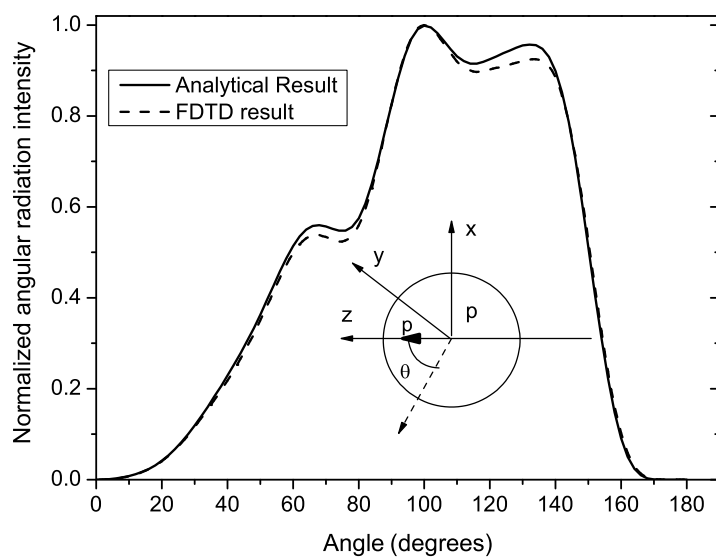
Fig. 35. Comparison of the angular radiation of a dipole at the half of the radius position with radial direction.

field angular radiation intensity of dipoles inside the cube and the cylinder are computed. The refractive indices of the cube and the cylinder are all 1.33; the wavelength is 6.28 µm; the width of the cube is 12.9 µm; the radius of the cylinder is 6.99 µm and the height of the cylinder is twice of its radius. Both the cube and the cylinder have the same volume as a sphere with radius of 8.0 µm. As in the previous case, we use normalized values of the intensity (normalized to the maximum value of the intensity). Fig. 36(a) shows the result for the radiation from a centered dipole inside the homogenous cube, and in Fig. 36(b) is the result of radiation from a centered dipole inside a homogenous cylinder. The direction of these dipoles are along the z axis as shown in the figure. Since the cube is not rotationally symmetric, our results show the radiation vs. polar angle (θ) at azimuthal angle $\phi = 0$. Results from FDTD and DDA are consistent.

C.   Conclusion

We developed a powerful and accurate method to simulate infinitesimal electric dipole radiation within particles with arbitrary shapes and internal compositions. The dipole direction can also be chosen arbitrarily. Although DDA can be used to simulate the dipole radiation more directly since it itself is based on a discrete dipole model, to simulate dipoles by FDTD has more simulating capabilities:

- For comparable accuracy, the FDTD can simulate larger size models than the DDA.

- FDTD simulation can give the temporal dipole field inside the particle where is the DDA can not.
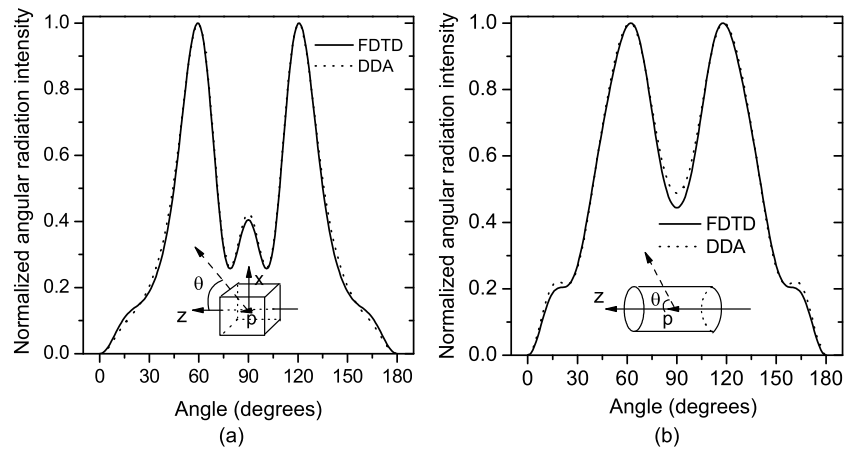
Fig. 36. Radiation from the dipole inside cube and cylinder which has a volume effective size parameter 8. In both cases, the direction of the dipole is along the z axis, the refractive index m=1.33 : (a) Normalized angular radiation intensity vs. polar angle for a centered dipole inside the homogenous cube; (b) Normalized angular radiation intensity vs. polar angle for a centered dipole inside the homogenous cylinder

With the method described in this chapter, coupled with the capability that FDTD can simulate internal radiative energy distribution as in Chapter VI, one can now study induced Raman scattering and fluorescence phenomena.

CHAPTER VIII

RADIATIVE COUPLING OF THE ATMOSPHERE-OCEAN SYSTEM

All we discussed before focused on radiative interactions with a single particle. Radiative interactions with turbid media which consist of large number of scatterers are very different. The multiple scattering usually governs this region. Radiative transfer in this region depends on several parameters: the absorption coefficient, the scattering coefficient, the single particle Mueller matrix, etc. These parameters can be determined when the optical properties of the single particle, the density distribution of the particles and their orientations are known. The techniques described in previous chapters are very powerful methods to calculate optical properties of small particles with arbitrary shapes and internal dielectric structures.

Our earth is covered by vast volumes of the gaseous layer, called the atmosphere, which extends from the ground to tens of kilometers high. The atmosphere is not a homogenous layer even in the clearest sky condition. Besides many types of clouds, dust particles, aerosols, water vapor and many other types materials are present in the atmosphere. Sunlight will unavoidably undergo multiple scattering and absorption by these constituents. On the other hand, more than 70% of the earth's surface is covered by ocean, specular reflections will occur even when the sunlight passes through the atmosphere. The ocean body is also another kind of turbid medium, which is not simply pure water. The light in the ocean also undergoes severe multiple scattering and absorption not only by the water molecule's density variation, but also by mineral particles, air bubbles, plankton, etc. We also need to understand that the stochastic interface separating the atmosphere from the ocean plays an importance role of the radiative transfer in the atmosphere-ocean system. Most earlier research has focused on studying radiative transfer in the atmosphere. Among them, Discrete ordinates

Radiative Transfer (DISORT)[4, 53] and Vector DISORT (VDISORT)[54, 55] are commonly used in studying horizontally homogenous models, and the Monte Carlo method have been used in studying radiative transfer in clouds [56, 57].

To study the radiative transfer in a complete atmosphere-ocean system, we separate the system into three layers as shown in Fig. 37: the atmosphere layer, the ocean layer and the ocean surface layer, which lies between the first two layers. We will study each layer and get the reflection and transmission properties of each of them separately, then a method called Matrix operator method [58, 59] will be applied to couple these layers' optical properties and construct a complete radiative interaction system.
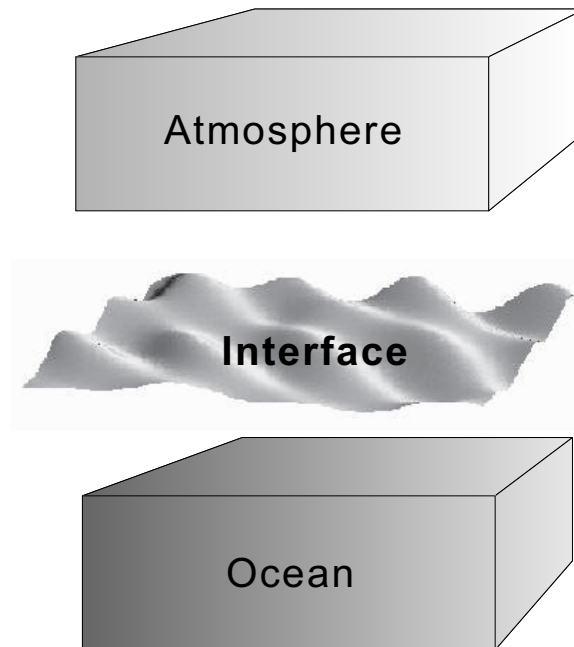
Fig. 37. The atmosphere-ocean system.

A. Radiative interaction with a single layer medium

As shown in Fig. 38, a light source, such as the sunlight, is illuminating on a medium (such as the atmosphere). The layer contains large number of isolated particles. We assume the refractive index is same both inside and outside the layer. Beer's law (Eq. 8.1) tells us how the radiance of the light that passes though the layer without deflection is attenuated,

$$I_{out} = I_{inc}e^{-\tau/cos(\theta)} \tag{8.1}$$

where τ is the optical depth of the layer and θ is the relative angle between the source direction and the normal direction of the layer surface. These energy lost in the original direction is due to the light absorption and scattering by the particles in the medium, as well as the absorption from the background medium.
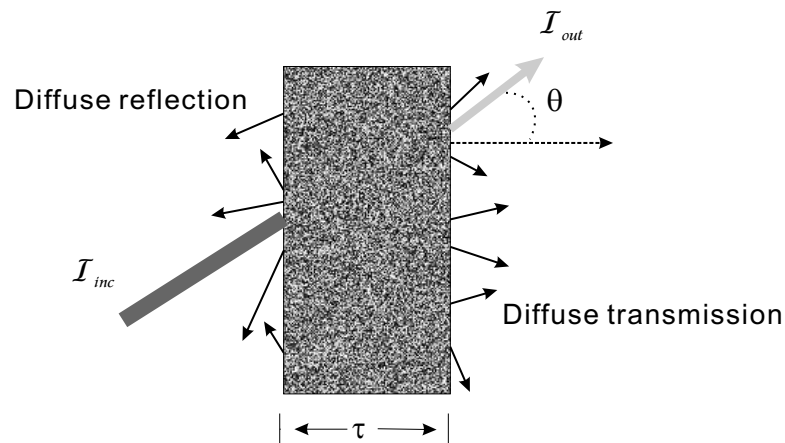
Fig. 38. Radiative interaction with a single layer medium.

Multiple scattering changes the photons' direction while they are traveling through the medium. In general, after multiple scattering, both transmitted and reflected radiation become diffuse. The diffuse radiation field can be in all directions, and it is usually denoted as radiance as described in Chapter I.

Another optical property of the radiation field is the polarization as was introduced in Chapter I. To completely describe the interactions with a single layer of medium, the polarization states of the source, the diffuse reflection, and the diffuse transmission are all needed to be take into account. In the following, we will first study the scalar field, then we will show what differences are incurred when one uses the vector field.

B.   Two layer coupling

Before we begin discussing the multi-layer coupling, we first analyze the optical properties of a single layer. As shown in Fig. 39, Z_0 and Z_1 represent the top and the bottom surface of the layer respectively. Both the top and the bottom surfaces are discretized by spatial grids. We also discretized the angular space, θ_i, (i=1,2...N) and ϕ_j, (j=1,2,....,M). Let us denote $F(\mathbf{r}_i, \hat{\mathbf{s}}_j)$ as the irradiance contained in $\Delta\Omega_j$ at the position $\mathbf{r}_i$, which is defined as $F(\mathbf{r}_i, \hat{\mathbf{s}}) = L(\mathbf{r}_i, \hat{\mathbf{s}})\Delta\Omega_j$, where L is radiance and $\Delta\Omega_j$ comes from the discretized angular space. For plane wave, the radiance is a delta function in angular space, then F means the plane irradiance. As described in the previous section, given an incident light source, the multiple scattering inside the medium will generate diffuse reflection on the top surface and diffuse transmission on the bottom surface at all spatial grids and in all directions.

A matrix form can be written down based on this spatially and angularly discretized space to represent the impulse response of an arbitrary source beam. For the reflection matrix:

$$r = \begin{pmatrix} \alpha_{1,1} & \cdots & \alpha_{1,n} \\ \vdots & \ddots & \vdots \\ \alpha_{n,1} & \cdots & \alpha_{n,n} \end{pmatrix}, \; \alpha_{i,j} = \begin{pmatrix} \alpha_{i,j}(s_1, s_1) & \cdots & \alpha_{i,j}(s_1, s_m) \\ \vdots & \ddots & \vdots \\ \alpha_{i,j}(s_m, s_1) & \cdots & \alpha_{i,j}(s_m, s_m) \end{pmatrix} \quad (8.2)$$
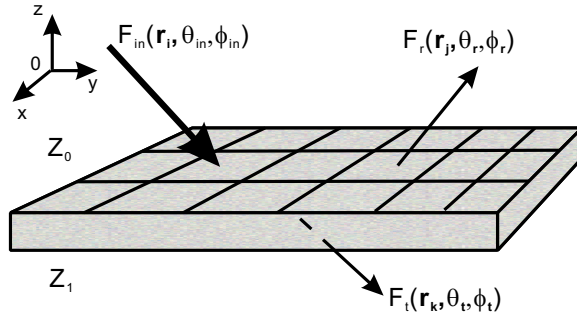
Fig. 39. A single layer model.

and the transmission matrix:

$$t = \begin{pmatrix} \beta_{1,1} & \cdots & \beta_{1,n} \\ \vdots & \ddots & \vdots \\ \beta_{n,1} & \cdots & \beta_{n,n} \end{pmatrix}, \ \beta_{i,j} = \begin{pmatrix} \beta_{i,j}(s_1, s_1) & \cdots & \beta_{i,j}(s_1, s_m) \\ \vdots & \ddots & \vdots \\ \beta_{i,j}(s_m, s_1) & \cdots & \beta_{i,j}(s_m, s_m) \end{pmatrix} \quad (8.3)$$

where the subscript of $\alpha_{i,j}$ and $\beta_{i,j}$ correspond to the spatial position r_i and r_j; the variable s_k corresponds to the discretized direction in angular space. The reflection matrix and transmission matrix act like operators in the sense that:

$$\mathbf{F}_r = r\mathbf{F}_{in}, \ \mathbf{F}_t = t\mathbf{F}_{in}, \ \mathbf{F} = \begin{pmatrix} F_1 \\ \vdots \\ F_n \end{pmatrix}, \ F_i = \begin{pmatrix} f_i(s_1) \\ \vdots \\ f_i(s_m) \end{pmatrix} \quad (8.4)$$

where $f_i(s_j)$ is the irradiance contained in $\Delta\Omega_j$ at position r_i.

There are several ways to get the matrix information; however the Monte Carlo method is the most robust to simulate very heterogenous media which are precisely the situation we are dealing with.

Unlike the single layer case, for two-layer model as shown in Fig. 40, the combined transmission and reflection of the two layer system involves the multiple scattering effects between layers. After simple mathematical derivations, the complete formula

of the combined transmission and reflection for two-layer system are:
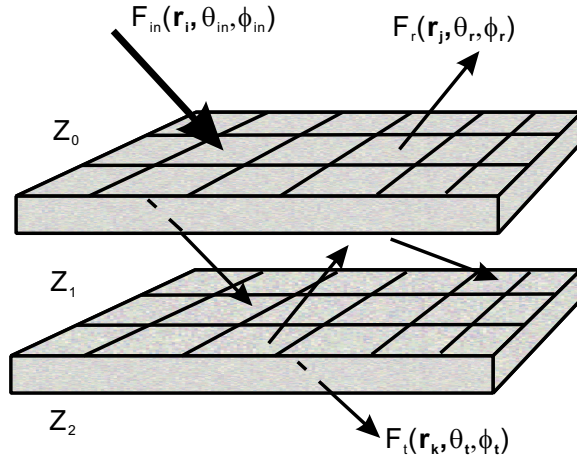
Fig. 40. A two layer coupling model.

$$r_{02} = r_{01} + t_{01} \left(E - r_{12}r_{10} \right)^{-1} r_{12}t_{01}$$

$$t_{02} = t_{12} \left(E - r_{12}r_{10} \right)^{-1} t_{01}$$

(8.5)

$$r_{20} = r_{21} + t_{12} \left(E - r_{10}r_{12} \right)^{-1} r_{10}t_{21}$$

$$t_{20} = t_{10} \left(E - r_{10}r_{12} \right)^{-1} t_{21}$$

(8.6)

where the subscripts in $r_{i,j}$ and $t_{i,j}$ mean the reflection and transmission matrix are of the layer that is between surface i and j, and the source illuminating direction points from surface i to surface j; E is the unit matrix. Eq. 8.5 and 8.6 correspond to two different combined results with the source beam illuminating from above Z_0 and below Z_2 respectively. If the two layers are all same homogenous layers, the two results are same. In general, these two results are different.

Eq. 8.5 and Eq. 8.6 are basic equations in the Matrix Operator Method. From two-layer results, it is straightforward to calculate systems with more layers. Thus the Matrix Operator Method can be used to study radiative coupling in multi-layer

systems by using matrix operations with the reflection and transmission matrices of each single layer.

The dimensionality of these matrices will be quite large considering all the information contained in them. Matrix operations in Eq. 8.5 and Eq. 8.6 all involve the operation of large matrix inverse, which is a major computational problem to calculate exactly. We therefore use an approximate calculation method to expand the matrix inverse term in a series:

$$\frac{1}{E - r_i r_j} = E + r_i r_j + (r_i r_j)^2 + \cdots + (r_i r_j)^n + \cdots \tag{8.7}$$

Usually several terms are good enough since the element values in diffuse reflection matrix are generally small for both atmosphere and ocean.

C. Matrix operator coupling results for scalar fields

We used the simplest model to test our Matrix Operator Method. Two semi-infinite layers are chosen. Each layer is homogenous with the optical depth of $\tau = 0.25$. We also set the scattering to Rayleigh scattering and the single scattering albedo ω_0=1.0 (conservative scattering). The light source is plane parallel normal incident light, with uniformly irradiance $F = 1W/m^2$. In our calculation, the 2π azimuthal angle is evenly divided into 20 pieces and the cosine polar angle is also discretized by 20 according to $cos(\theta) = 1.0,\ 0.9,\ \cdots,\ -0.9,\ -1.0$. The single layer reflection and transmission matrices are calculated from the DISORT method. In Fig. 41, we compute the combined results of two layers by Matrix Operator Method and compare our results with the DISORT method. The angle used in Fig. 41 is the relative angle between the reflected or the transmitted light with the the normal direction. The term "order" means the highest power order expanded in Eq. 8.7.
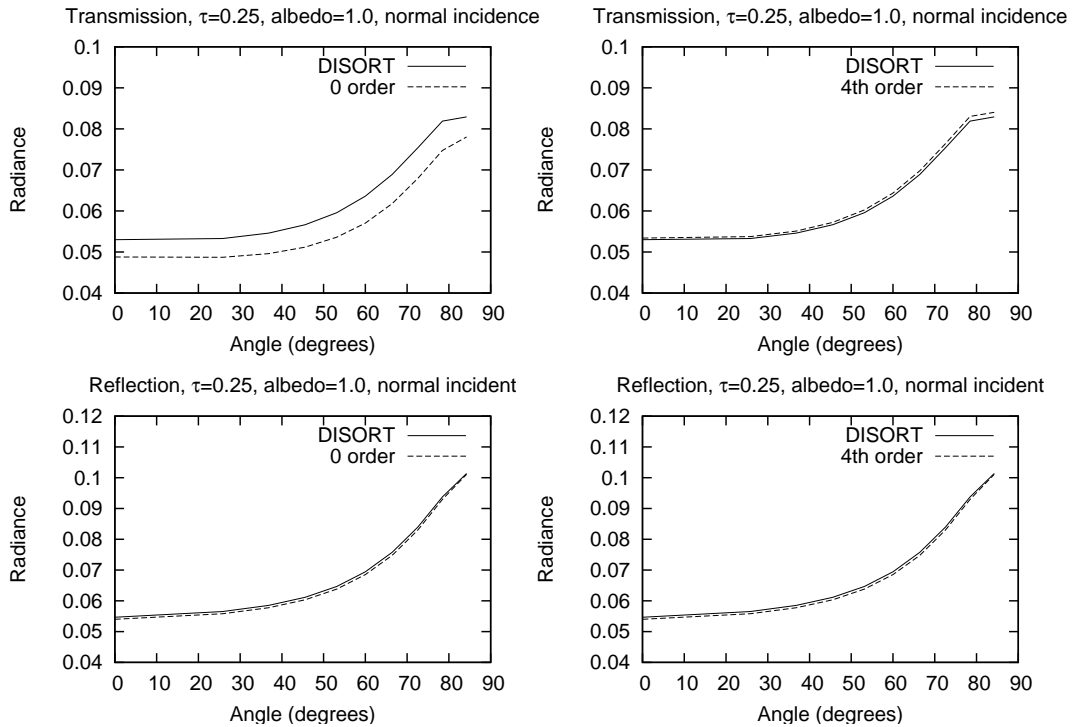
Fig. 41. Comparison with DISORT

In this simple example as a 1D model, the Matrix Operator Method shows its high accuracy.

D. Scalar field and vector field

The radiation field is a vector field, the reflection and transmission radiance not only depend on the incident irradiance, but also depend on the polarization state of the source. As described in Chapter I, the complete description of vector radiation field is in terms of Stokes vector, and the Mueller matrix is the matrix connecting the incident wave with the scattered wave. To fully explore the optical properties of the layer, the reflection and transmission matrices need to be modified. Firstly, the matrix elements in the reflection matrix and transmission matrix of Eq. 8.2,8.3 need

to be modified as:

$$\alpha_{i,j}(s_k, s_l), \beta_{i,j}(s_k, s_l) = \begin{pmatrix} m_{11} & m_{12} & m_{13} & m_{14} \\ m_{21} & m_{22} & m_{23} & m_{24} \\ m_{31} & m_{32} & m_{33} & m_{34} \\ m_{41} & m_{42} & m_{43} & m_{44} \end{pmatrix} \tag{8.8}$$

and the vector elements in Eq. 8.4 are also needed to be replaced by Stokes vector as:

$$f_i(s_j) = \begin{pmatrix} I_i(s_j) \\ Q_i(s_j) \\ U_i(s_j) \\ V_i(s_j) \end{pmatrix} \tag{8.9}$$

In Fig. 42, we compared the reflected radiance for both the scalar field and the vector field. The simulation is for a single layer with optical depth $\tau = 1.0$, Rayleigh scattering with albedo 1.0. The light source is unpolarized plane sunlight with normal incidence. The angle parameter in figure is the relative angle to the normal direction. The radiances are obviously different between these two cases. Thus the polarization must be considered in order to simulate radiative transfer for electromagnetic waves.

E.   Refractive index mismatched interface

As it is well known, Fresnel's law describes the reflection and transmission of the electromagnetic waves at the interface between two media with difference refractive indices. In derivation of the Fresnel's law, plane waves are used for the electromagnetic field in both media. To study the radiance defined in Chapter I, one needs carefully exam the physical meaning in Fresnel's Law. As shown in Fig. 43, two media with refractive indices n_1 and n_2 respectively are connected at the a surface. Two different
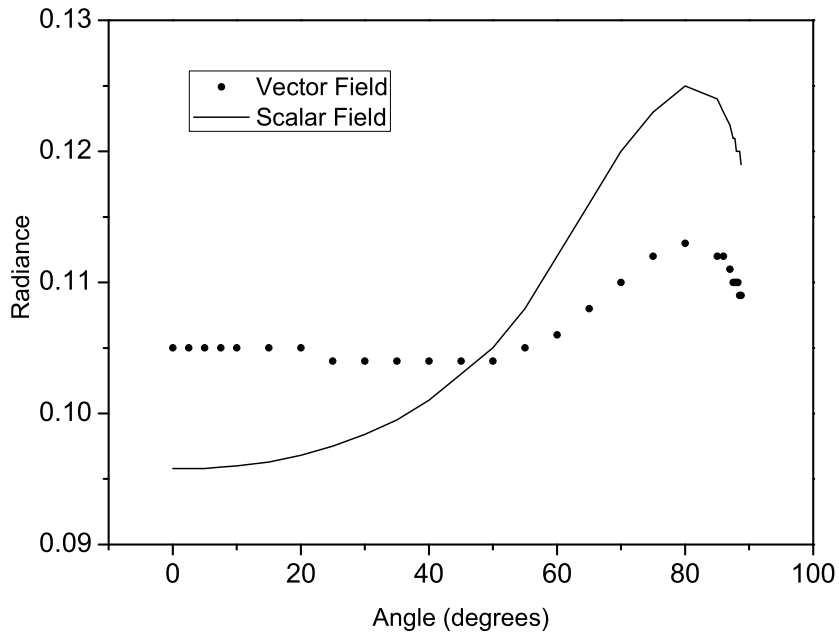
Fig. 42. Comparison of the vector field and scalar field for the transmitted radiance.

incident light sources are presented: the diffuse light source (denoted by radiance)in the left and the plane wave source (plane parallel light denoted by irradiance)in the right. We don't show the specular reflection which is simple to include.

Defining the relative refractive index as $n = n_2/n_1$, and assuming the incident angle and refractive angle are θ and θ' respectively. We also define the transmission coefficient T means the ratio of the transmitted energy flux to the incident flux for plane wave as show in Fig. 43:

$$I_2 \ cos(\theta') = T I_1 \ cos(\theta) \tag{8.10}$$

where I_1 and I_2 are plane irradiance of the incident light and transmitted light. In
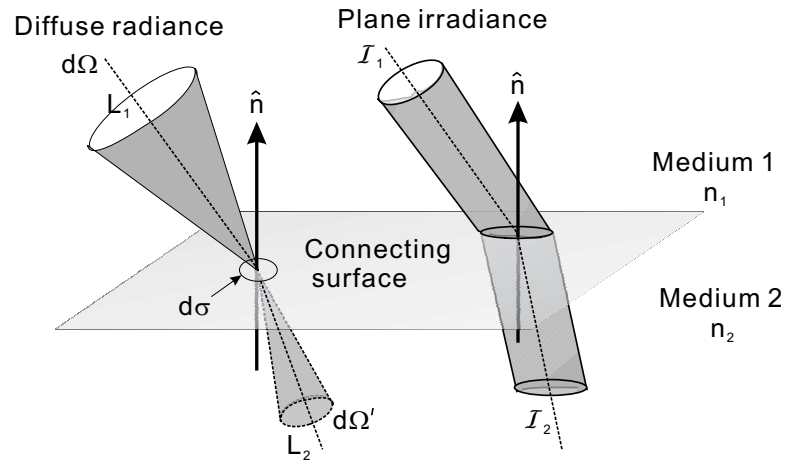
Fig. 43. Refraction of diffuse light and plane wave.

case of the radiance, the transmitted energy flux through the small area $d\sigma$ has the following equation:

$$L'cos(\theta')d\Omega'd\sigma = TLcos(\theta)d\Omega d\sigma \tag{8.11}$$

where $d\Omega' = sin(\theta')d\theta'd\phi$ and $d\Omega = sin(\theta)d\theta d\phi$. Then after cancelling same factors on both sides of the above equation, one can obtain:

$$L'cos(\theta')dcos(\theta') = TLcos(\theta)dcos(\theta) \tag{8.12}$$

From Snell's law:

$$n\ sin(\theta') = sin(\theta) \tag{8.13}$$

After some algebra, we obtain:

$$n^2cos(\theta')dcos(\theta') = cos(\theta)dcos(\theta) \tag{8.14}$$

Substituting the above relation into Eq. 8.12, the relation between the two radiances can be obtained:

$$L' = n^2TL \tag{8.15}$$

Now one can see the relation between incident and transmitted radiance is very different compared with the relation between irradiance of the incident and the transmitted plane wave as shown in Eq. 8.10.

In our coupling model of the atmosphere-ocean system, as in Fig. 37, the ocean surface itself forms a layer. As described earlier in this chapter, optical properties of a layer are presented in terms of its reflection and transmission matrices. To calculate the transmission matrix of an ocean surface layer, Eq. 8.15 must be used.

Another special feature of the refractive index mismatched surface is the total internal reflection, which occurs when light travels from a larger refractive index medium to a smaller index medium. This also needs to be carefully considered when constructing matrices for the ocean surface layer.

F.   Conclusions and future plans

We have shown the basic idea of the Matrix operator method, and tested the method in a simple case. Our ultimate goal is to get a time dependent radiative coupling method for an atmosphere-ocean system based on the Matrix operator method. Although many other methods, such as DISORT, are being used in studying radiative transfer in atmosphere systems, which are only valid for horizontally homogenous layers. This research work is just in its early stage, to reach our goal, three more important steps are needed:

1. Both matrices and the operations need to be modified for the vector radiation field.

2. Appropriate mathematical ocean surface model is needed, which is essential to construct the matrix for the ocean surface layer.

3. A fast computing algorithm is needed for handling very large matrices.

Once the complete Matrix operator method of the atmosphere-ocean system is done, we will not only be able to study the radiative transfer by the sunlight, but we will also be able to study the atmosphere and ocean using an active light source. A large number of applications can make use of these methods, such as image distortion by ocean surface, studying broken clouds, remote underwater detection, etc.

CHAPTER IX

SUMMARY

In this dissertation, we studied two categories of radiative interactions: interactions with a single small particle and interactions with media that contain large numbers of isolated particles. Both the scattering and emission interactions studied here are assumed to be classic and linear interactions that are all fully described in Maxwell's equations.

For the first kind of interaction, we focused on two regions: the elastic scattering by small particles and the radiation from infinitesimal electric dipoles embedded in small host particles. In both cases, the sizes of the particle are comparable with the wavelength, thus the geometric optics breaks down. The major numerical method we use is the Finite-Difference Time-Domain (FDTD) method. Based on previous FDTD code, we develop our own program to simulate interactions with different irregular particles. We also developed a parallel version FDTD code to simulate cases with large particles.

We studied both near field (radiative energy density distribution) and far field (surface roughness effects and Mueller images) in the elastic scattering region. In studying the radiative energy density distribution inside and in the vicinity of a particle with the plane-illuminating beam, our results show that the energy density distributions are sensitive to the shape and internal structure of particles, and the intensity could be magnified hundreds of times of the illuminating beam. In studying the effects of the surface roughness on the light scattering, we first defined a parameter to describe the degree of roughness and then study the changes in the far field patterns with the roughness parameter increases. Our results show that when the roughness parameter is large enough, the light scattering by the roughened particle can no longer

be approximately treated as its overall shape in studying the light scattering. We also studied the Mueller images of irregular particles from the far field scattered light, we find backscattered Mueller images contain abundant information of the shapes and internal structures of the studied particles, which can be used to detect biological agents.

We presented an innovative method to simulate the radiation pertaining to the infinitesimal electric dipoles embedded in arbitrary shape and composition small particles. This method is very accurate in comparison with the analytical results. Simulation results also show the patterns of the radiation in the far field are highly sensitive to the shape of the particle and the position and orientation of the dipole, which can be used into particle detection. This method can also be used to study Raman scattering and fluorescence effects.

The second kind of radiative interactions studied is the radiative transfer in an atmosphere-ocean system. We separated the whole system into three layers: the atmosphere layer, the ocean surface layer and the ocean body. The optical properties of each layer (reflection and transmission) can be obtained from several different methods, such as DISORT, Monte Carlo, etc. Then the Matrix operator method is used to couple different layers together. In general, this method considers all orders of multiple scattering between layers. Although the method is at its early stage, from the several simple cases we present, this method is very accurate and can handle both the radiance and polarization of the radiation field. We also stated the difficulties of this method and discussed possible research directions for future works.

REFERENCES

[1] K. N. Liou,Y. Takano,and P. Yang, "Light scattering and radiative transfer by ice crystal clouds: Applications to climate research," in *Light Scattering by Nonspherical Particles: Theory, Measurements, and Geophysical Applications*, M. I. Mishchenko, J. W. Hovenier, and L. D. Travis, eds.(Academic Press, New York, 2000), pp. 417-449.

[2] M. I. Mishchenko, L. D. Travis, and D. W. Mackowski, "T-matrix computations of light scattering by nonspherical particles: a review," J. Quant. Spectrosc. Radiat. Transfer **55**, 535-575 (1996).

[3] H.C. van de Hulst, *Light Scattering by Small Particles* (Dover Publications, Inc, New York, NY, 1981).

[4] S. Chandrasekhar, *Radiative Transfer* (Dover Publications, Inc, New York, NY, 1960).

[5] K. S. Yee, "Numerical solution of initial boundary problems involving Maxwell's equations in isotropic media," IEEE Trans. Antennas. Propagat. **AP-14**, 302-307 (1966).

[6] A. Taflove and S. Hagness, *Computational Electrodynamics: The Finite-Difference Time-Domain Method* (Artech, Boston, MA, 2000).

[7] G. Mur, "Absorbing boundary conditons for the finite-difference approximation of the time-domain electromagnetic field equations," IEEE Trans. Electromag. Comp. **23**, 377-382 (1981).

[8] K. R. Umashankar, and A. Taflove, "A novel method to analyze electromagnetic scattering of complex objects," IEEE Trans. Electroman. Comp. **24**, 397-405 (1982).

[9] J, P. Berenger, "A perfectly matched layer for the absorption of electromagnetic waves," J. Comput. Phys. **114**, 185-200 (1994).

[10] Z. S. Sacks, D. M. Kingsland, R. Lee, and J. F. Lee, "A perfect matched anisotropic absorber for use as an absorbing boundary condition," IEEE Trans. Antennas. Propag. **43**, 1460-1463 (1995).

[11] S. A. Schelkunoff, "Some equivalence theorems of electromagnetics and their application to radiation problems," AT&T. Tech. J. **15**, 92-112 (1936).

[12] C. A. Balanis, *Advanced Engineering Electromagnetics* (Wiley, New York, 1989).

[13] W. Sun and Q. Fu, "Finite-difference time-domain solution of light scattering by dielectric particles with large complex refractive indices," Appl. Opt. **39**, 5569-5578, (2000).

[14] Marc Snir, Steve Otto, Steven Huss-Lederman, David Walker, and Jack Dongarra, *MPI-The Complete Reference: Volume 1, The MPI Core,* second edition (The MIT Press, Cambridge, MA 1998).

[15] Q. H. Liu, "The PSTD Algorithm: A time-domain method requiring only two cells per wavelength," Microwave. Opt. Techn. Lett. **15**, 158-165 (1997).

[16] Q. H. Liu, "Large-scale simulations of electromagnetic and acoustic measurements using the pseudospectral time-domain (PSTD) algorithm," IEEE Trans. Geosci. Remote Sensing **37**, 917-926 (1999).

[17] Y. L. Pan, K. B. Aptowicz, R. K. Chang, M. Hart, and J. D. Eversole, "Characterizing and monitoring respiratory aerosols by light scattering," Opt. Lett, **28**, 589-591 (2003).

[18] B. A. Wielicki, B. R. Barkstrom, B. A. Baum, T. P. Charlock, R. N. Green, D. P. Kratz, R . B. Lee, P. Minnis, G. L. Smith, Takmeng Wong, D. F. Young, R. D. Cess, J. A. Coakley, D. A. H. Crommelynck, L. Donner, R. Kandel, M. D. King, A. J. Miller, V. Ramanathan, D. A. Randall, L. L. Stowe, R. M. Welch, "Clouds and the Earth's Radiant Energy System (CERES): algorithm overview," IEEE Trans. Geosci. Remote Sensing **36**, 1127-1141 (1998).

[19] M. I. Mishchenko, J. W. Hovenier, L. D. Travis, *Light Scattering by Nonspherical Particles* (Academic Press, San Diego, CA, 2000).

[20] T. Wriedt, "A review of elastic light scattering theories," Part. Part. Syst. Charact. **15**, 67-74 (1998).

[21] A. Macke, J. Muller, and E. Rascke, "Single scattering properties of atmospheric ice crystals," J. Atmos. Sci. **53**, 2813-2825 (1996).

[22] P. Yang and K. N. Liou, "Single-scattering properties of complex ice crystals in terrestrial atmosphere," Contr. Atmos. Phys. **71**, 223-248(1998).

[23] R. Schiffer, "Light scattering by perfectly conducting statistically irregular particles," J. Opt. Soc. Am. A **6**, 385-402 (1989).

[24] R. Schiffer, "Perturbation approach for light scattering by an ensemble of irregular particles of arbitrary material," Appl. Opt. **29**, 1536-1550 (1990).

[25] K. Lumme and J. Rahola, "Comparison of light scattering by stochastically rough spheres, best-fit spheroids and spheres," J. Quant. Spectrosc. Radiat. Transfer

60, 439-450 (1998).

[26] T. Nousiainen, K. Muinonen, J. Avelin and A. Sihvola, "Microwave backscattering by nonspherical ice particles at 5.6 GHz using second-order perturbation series," J. Quant. Spectrosc. Radiat. Transfer **70**, 639-661 (2001).

[27] W. Sun, T. Nousiainen, K. Muinonen, Q. Fu, N. G. Loeb and G. Videen, "Light scattering by Gaussian particles: a solution with finite-difference time-domain technique," J. Quant. Spectrosc. Radiat. Transfer **79-80**, 1083-1090 (2003).

[28] K. Chamaillard and J. J. Lafon "Statistical approach of the effects of roughness on the polarization of light scattered by dust grains," J. Quant. Spectrosc. Radiat. Transfer **70**, 519-528 (2001).

[29] J. M. Perrin and J. P. Sivan, "Porosity and impurities within interstellar grains - Is the ultraviolet bump still explained by carbonaceous material?" Astron. Astrophys. **228**, 238-245 (1990).

[30] B. T. Draine, "The discrete-dipole approximation and its application to interstellar graphite grains," Astrophys. J. **333**, 848-872 (1988).

[31] B. T. Draine and P. J. Flatau, "Discret-dipole approximation for scattering calculations," J. Opt. Soc. Am. A. **11**, 1491-1499 (1994).

[32] W. Sun, N. G. Loeb, G. Videen, and Q. Fu, "Examination of surface roughness on light scattering by long ice columns by use of a two-dimensional finite-difference time-domain algorithm," Appl. Opt. **43**, 1957-1964 (2004).

[33] D. A. Henderson, "The looming threat of bioterrorism," Science **283**, 1279-1282 (1999).

[34] M. O. Scully, G. W. Kattawar, R. P. Lucht, T. Opatrny, H. Pilloff, A. Rebane, A. V. Sokolov, and M. S. Zubairy, "FAST CARS: Engineering a laser spectroscopic technique for rapid identification of bacterial spores," Proc. Natl. Acad. Sci. USA. **99**, 10994-11001(2002).

[35] R. G. Pinnick, S. C. Hill, P. Nachman, J. D. Pendleton, G. L. Fernandez, M. W. Mayo, and J. G. Bruno, "Fluorescence particle counter for detecting airborne bacteria and other biological particles," Aerosol. Sci. Tech. **23**, 653-664 (1995).

[36] B. D. Cameron, M. J. Rakovic, M. Mehrbeoglu, G. W. Kattawar, S. Rastegar, L. V. Wang, and G. L. Cot, "Measurement and calculation of the two-dimensional backscattering Mueller matrix of a turbid medium," Opt. Lett. **23**, 485-487 (1998).

[37] A. A. Nezhuvingal, Y. Li, H. Anumula, B. D. Cameron, "Mueller matrix optical imaging with application to tissue diagnostics," Proc. SPIE. **4961**, 67-146 (2003).

[38] Philip J. Wyatt, "Differential light scattering: a physical method for identifying living bacterial cells," Appl. Opt. **7**, 1879-1896 (1968).

[39] D. S. Benincasa, P. W. Barber, J.-Z. Zhang, W. -F. Hsieh, and R. K. Chang, "Spatial distribution of the internal and near-field intensities of large cylindrical and spherical scatterers," Appl. Opt. **26**, 1348-1356 (1987).

[40] J. F. Owen, R. K. Chang and P. W. Barber, "Internal electric field distributions of a dielectric cylinder at resonance wavelengths," Opt. Lett. **6**, 540-542 (1981).

[41] L. G. Astafyeva, V. A. Babenko, "Interaction of electromagnetic radiation with silicate spheroidal aerosol particles," J. Quant. Spectrosc. Radiat. Transfer. **88**, 9-15 (2004).

[42] J. P. Barton, "Electromagnetic field calculations for an irregularly shaped, near-spheroidal particle with arbitrary illumination," J. Opt. Soc. Am. A **19**, 2429-2435 (2002).

[43] Yang, P., K. N. Liou, M. I. Mishchenko, and B.-C. Gao, "An efficient finite-difference time domain scheme for light scattering by dielectric particles: application to aerosols," Appl. Opt. **39**, 3727-3737 (2000).

[44] W. Sun, Q. Fu, and Z. Chen, "Finite-difference time-domain solution of light scattering by dielectric particles with perfectly matched layer absorbing boundary conditions," Appl. Opt. **38**, 3141-3151 (1999).

[45] M. I. Mishchenko, J. W. Hovenier, and L. D. Travis, Eds. *Light Scattering by Nonspherical Particles* (Academic Press, San Diego, CA, 2000).

[46] C. Li, G. W. Kattawar and P. Yang, "Effects of surface roughness on light scattering by small particles," J. Quant. Spectrosc. Radiat. Transfer. **89**, 123-131 (2004).

[47] J. D. Jackson, *Classical Electrodynamics* (John Wiley and Sons Inc, New York, 1998).

[48] Z. Chen, A. Taflove, "Photonic nanojet enhancement of backscattering of light by nanoparticles: a potential novel visiblelight ultramicroscopy technique," Opt. Express. **12**, 1214-1220 (2004).

[49] E. Betzig and J. K. Trautman, "Near-field optics: Microscopy, spectroscopy, and surface modification beyond the diffraction limit," Science **257**, 189-195 (1992).

[50] H. Chew, P. J. McNulty, and M. Kerker, "Model for Raman and fluorescent scattering by molecules embedded in small particles," Phys. Rev. A. **13**, 396-404

(1976).

[51] H. Chew, "Transition rates of atoms near spherical surfaces," J. Chem. Phys. **87**, 1355-1360 (1987).

[52] H. Chew, "Radiation lifetime of atomos inside dielectric particles," Phys. Rev. A. **38**, 3410-3416 (1988).

[53] K. N. Liou, "A numerical experiment on Chandrasekhar's discrete-ordinates method for radiative transfer: Application to cloudy and hazy atmospheres," J. Atmos. Sci. **30**, 1303-1326 (1973).

[54] F. Wen, "A multi-layer discrete-ordiate method for vector radiative transfer in a vertically-inhoogenous, emitting and scattering atmosphere-I. theory," J. Quant. Spectrosc. Radiat. Transfer **47**, 19-33 (1992).

[55] F. Wen, "A multi-layer discrete-ordiate method for vector radiative transfer in a vertically-inhoogenous, emitting and scattering atmosphere-II. application," J. Quant. Spectrosc. Radiat. Transfer **47**, 35-42 (1992).

[56] L. Roberti and C. Kummerow, "Monte Carlo calculations of polarized microwave radiation emerging from cloud structures," J. Geophys. Res. **104**, 2093-2104 (1999).

[57] C. Davis, C. Emde, and R. Harwood, "A 3-D polarized reversed Monte Carlo radiative transfer model for Millimeter and submillimeter passive remote sensing in cloudy atmospheres," IEEE Trans. Geosci. Remote Sensing **43**, 1096-1101 (2004).

[58] G. N. Plass, G. W. Kattawar and F. E. Catchings, "Matrix operator theory of radiative transfer I. Rayleigh scattering," Appl. Opt. **12**, 314-329 (1973).

[59] G. W. Kattawar, G. N. Plass and F. E. Catchings, "Matrix operator theory of radiative transfer. II. Scattering from maritime haze," Appl. Opt. **12**, 1071-1084 (1973).

APPENDIX A

1D FDTD BOUNDARY CONDITION

The two ends points in Fig. 3 are only used in updating the magnetic fields' values for $H(0.5)$ and $H(11.5)$. In this appendix, we gave a simple example for the boundary condition used in 1D FDTD, the following is a section of the code.

BEGIN PROGRAM

.

.

.

ELS1 = 0.0

ELS2 = 0.0

ERS1 = 0.0

ERS2 = 0.0

DO NTIME=1, TOTAL_TIME ! TIME LOOP

Updating E fields

ELS1 = E(1)

ELS2 = ELS1

E(0) = ELS2

ERS1 = E(11)

ERS2 = ERS1

E(12) = ERS2

Updating H fields

END DO

.

.

.

The program structure above guaranties that the at the time to temporally updating magnetic field values of H(0.5) and H(11.5), the electric field values for two ends are same as values of nearby grid (E(1) and E(11)) values of two time intervals ago.

APPENDIX B

FDTD

In Chapter II, there are two coefficients in electric field updating terms Eqs. 2.12, 2.13 and 2.14. Our scheme in FDTD used the following expressions:

$$\gamma(\mathbf{r}) = \frac{2\pi c \Delta t}{\lambda} \frac{\epsilon_i(\mathbf{r})}{\epsilon_r(\mathbf{r})} \tag{B.1}$$

where c is the speed of light in vacuum, λ is the wavelength in vacuum, ϵ_r and ϵ_i is the real and imaginary parts of the permittivity. Δt is the temporal interval in the FDTD simulation. With the γ defined above, the coefficients used in electric fields updating are:

$$a(\mathbf{r}) = e^{-\gamma(\mathbf{r})} \tag{B.2}$$

and

$$b(\mathbf{r}) = \frac{c\Delta t}{\Delta x} \frac{1 - a(\mathbf{r})}{\gamma(\mathbf{r})\epsilon_r(\mathbf{r})}. \tag{B.3}$$

In case of the very small γ, such as small absorption, we used:

$$b(\mathbf{r}) = \frac{c\Delta t}{\Delta x \epsilon_r(\mathbf{r})} \left[1.0 - \frac{\gamma}{2}(1 - \frac{\gamma}{3}(1 - \frac{\gamma}{4})) \right] \tag{B.4}$$

to reduce the numerical error.

APPENDIX C

DIPOLE RADIATION FORMULA

In this appendix, we gave explicit expression of the radiation electrical field due to the infinitesimal dipole. It is assumed that the dipole is placed in a medium with permittivity of ϵ and permeability of μ. The speed of the light in that medium is c, and the distance from the dipole is r. The coordination system is a Cartesian system.

$$p(t) = (\alpha_x \hat{x} + \alpha_y \hat{y} + \alpha_z \hat{z})e^{-\beta(T_0 - t)^2} \tag{C.1}$$

where α_x, α_y and α_z are amplitude parameters of the dipole in three directions, β is the parameter to control the Gaussian shape of the dipole function and $\beta = 1/\sigma^2$. T_0 is a preset time delay. The derivation of the explicit expressions for electric fields according to Eqs. 7.2, 7.3, 7.4 is complicated. We used Mathematica to do the calculation and the results are shown in the following:

$$
\begin{aligned}
E_x(\mathbf{r}, t) = \frac{e^{-\beta[r+c(T_0-t)]^2/c^2}}{8\pi\epsilon\beta c^4 r^5} &\left[-(3c^4 + 4\beta^2 r^4 + 4\beta c^2 r^2(1 + \beta(t - T_0)^2)\right. \\
&+ 6\beta c^3 r(T_0 - t) + 8\beta^2 c r^3(T_0 - t))x(\alpha_y y + \alpha_z z) \\
&+ \alpha_x(4\beta^2 r^4(y^2 + z^2) - 8\beta^2 c r^3(t - T_0)(y^2 + z^2) \\
&+ 2\beta c^3 r(t - T_0)(2r^2 - 3(y^2 + z^2)) + c^4(-2r^2 + 3(y^2 + z^2)) \\
&\left.+ 4\beta c^2 r^2(-r^2 + (1 + \beta(t - T_0)^2)(y^2 + z^2)))\right]
\end{aligned}
\tag{C.2}
$$

$$E_y(\mathbf{r}, t) = \frac{e^{-\beta[r+c(T_0-t)]^2/c^2}}{8\pi\epsilon\beta c^4 r^5} \left[-((3c^4 + 4\beta^2 r^4 + 4\beta c^2 r^2 (1 + \beta(t-T_0)^2) \right.$$

$$+6\beta c^3 r(T_0 - t) + 8\beta^2 cr^3(T_0 - t))y(\alpha_a xx + \alpha_a zz))$$

$$+\alpha_a y(4\beta^2 r^4(x^2 + z^2) - 8\beta^2 cr^3(t - T_0)(x^2 + z^2)$$

$$+2\beta c^3 r(t - T_0)(2r^2 - 3(x^2 + z^2)) + c^4(-2r^2 + 3(x^2 + z^2))$$

$$\left. +4\beta c^2 r^2(-r^2 + (1 + \beta(t-T_0)^2)(x^2 + z^2)))\right]$$

(C.3)

$$E_z(\mathbf{r}, t) = \frac{e^{-\beta[r+c(T_0-t)]^2/c^2}}{8\pi\epsilon\beta c^4 r^5} \left[-(3c^4 + 4\beta^2 r^4 + 4\beta c^2 r^2 (1 + \beta(t-T_0)^2) \right.$$

$$+6\beta c^3 r(T_0 - t) + 8\beta^2 cr^3(T_0 - t))(\alpha_x x + \alpha_y y)z$$

$$+\alpha_z(4\beta^2 r^4(x^2 + y^2) - 8\beta^2 cr^3(t - T_0)(x^2 + y^2)$$

$$+2\beta c^3 r(t - T_0)(2r^2 - 3(x^2 + y^2)) + c^4(-2r^2 + 3(x^2 + y^2))$$

$$\left. +4\beta c^2 r^2(-r^2 + (1 + \beta(t-T_0)^2)(x^2 + y^2)))\right]$$

(C.4)

VITA

Changhui Li

Permanent Address: WaiMao Gongsi Qihe, Shan Dong, 251100, China

Education:

    Bachelor of Science: Technical Physics, Peking University, Beijing, China 1997.

    Master of Science: Physics, Peking University, Beijing, China 2000.

    Master of Science: Physics, Texas A&M University, College Station, TX 2002.

    Awards: Regents Fellowship, Texas A&M University, 2000.

                      AUF Fellowship, Texas A&M University, 2001.

Publications:

1. C. Li, G. W. Kattawar, and P. Yang, Opt. Express **14**, 3616-3621 (2006).

2. C. Li, G. W. Kattawar, P. Zhai, and P. Yang, Opt. Express **13**, 4554-4559 (2005).

3. P. Zhai, G. W. Kattawar, P. Yang, and C. Li, Appl. Opt. **44**, 1650-1656 (2005).

4. C. Li, G. W. Kattawar, P. Yang, J. Quant. Spectrosc. Radiat. Transfer **89**, 123-131 (2004).

5. C. Li, G. W. Kattawar, P. Yang, J. of Electromagnetic. Wave. **18**, 797-806 (2004).

6. C. H. Li, C. M. Ko, Nucl. Phys. A **712**, 110-130 (2002).

7. C. Li, H. Ding, J. Dai, X. Song, Commun. Theor. Phys. **35**, 441-446 (2001).

8. G. Hua, C. Li, Q. Wang, Q. Zhang, J. Phys. G **24**, 125-133 (1998).